



저작자표시-비영리-변경금지 2.0 대한민국

이용자는 아래의 조건을 따르는 경우에 한하여 자유롭게

- 이 저작물을 복제, 배포, 전송, 전시, 공연 및 방송할 수 있습니다.

다음과 같은 조건을 따라야 합니다:



저작자표시. 귀하는 원저작자를 표시하여야 합니다.



비영리. 귀하는 이 저작물을 영리 목적으로 이용할 수 없습니다.



변경금지. 귀하는 이 저작물을 개작, 변형 또는 가공할 수 없습니다.

- 귀하는, 이 저작물의 재이용이나 배포의 경우, 이 저작물에 적용된 이용허락조건을 명확하게 나타내어야 합니다.
- 저작권자로부터 별도의 허가를 받으면 이러한 조건들은 적용되지 않습니다.

저작권법에 따른 이용자의 권리는 위의 내용에 의하여 영향을 받지 않습니다.

이것은 [이용허락규약\(Legal Code\)](#)을 이해하기 쉽게 요약한 것입니다.

[Disclaimer](#)

Ph.D. DISSERTATION

**Plasma induced dewetting of  
solid state metal films  
for nanostructure applications**

**Changhee Choe**

February 2016

Department of Materials Science and Engineering

College of Engineering

Seoul National University

# Plasma induced dewetting of solid state metal films for nanostructure applications

Advisor Prof. Jung-Joong Lee

Submitting a Ph.D. Dissertation of Public Administration

Department of Materials Science and Engineering  
College of Engineering  
Seoul National University

**Changhee Choe**

February 2016

Confirming the Ph.D. Dissertation written by

**Changhee Choe**

|            |                 |        |
|------------|-----------------|--------|
| Chair      | Dongil Kwon     | (Seal) |
| Vice Chair | Jung-Joong Lee  | (Seal) |
| Examiner   | Nong-moon Hwang | (Seal) |
| Examiner   | Sang Yul Lee    | (Seal) |
| Examiner   | Dong-Hoon Han   | (Seal) |

# Abstract

During solid-state dewetting, a physical phenomenon, thin films disintegrate into a set of droplets or particles at temperatures below the melting temperature. Plasma-induced dewetting, in contrast to thermal dewetting and pulsed-laser dewetting, is a rapid process that can be performed at low temperatures and over large-scaled areas. In addition, more uniform nanoparticle arrays can be fabricated (compared to those obtained via thermal dewetting) owing to the high density of holes nucleated during this process, which prevents the coarsening of nanoparticles.

In this research, various metal nanoparticle arrays (Au, Ag, Cu) are fabricated using inductively coupled plasma and the mechanism of plasma-induced dewetting is discussed. The evolution of solid-state dewetting with plasma treatment time is examined. Furthermore, the open area of metallic films is calculated through image analysis of images obtained via field emission scanning electron microscopy (FE-SEM). The crystallographic evolution during dewetting is examined by using grazing-incidence small-angle X-ray scattering.

Various parameters such as the film thickness, plasma treatment time, film density, and the interfacial energy between the film and the

substrate are considered. The size, inter-particle spacing, and number of nanoparticles per unit-area are modified by varying these parameters. More importantly, a repeated dewetting process method that leads to significant changes in the nanoparticle array distribution is introduced.

The nanoparticle array and bi-continuous nano-film fabricated by using the plasma-induced dewetting method are used for various applications such as organic solar cells, photocatalytic activity of  $\text{TiO}_2$ , and transparent conductive electrodes materials. A Au-nanoparticle array on indium tin oxide (ITO) is used to improve the performance of organic solar cells via the plasmon-enhanced absorption effect. Moreover, the features of the array are varied in order to promote overlapping of the active layer absorption band and the Au nanoparticle plasmonic resonance frequency; an optimum condition is suggested in order to maximize the power conversion efficiency via the near-field effect.

The Au-nanoparticle array is also used to enhance the efficiency of the system, by means of the photocatalytic activity. The photocatalytic activity of Au nanoparticles(NPs)/ $\text{TiO}_2$  was evaluated by determining the photo-degradation of methylene blue (MB) under ultraviolet (UV) or visible-light irradiation.

In addition to the nanoparticle array, a bi-continuous Au nano-film is used in transparent conductive electrodes (TCE) that are essential for

providing electrical contact and transmittance for solar cells and display devices. The sheet resistance ( $R_s$ ) and optical transmittance (T), which are key parameters of TCE, are determined by the thickness of the Au film and the plasma treatment time, respectively. The plasma-induced dewetting method constitutes a simple, fast, and efficient process for the fabrication of continuous metal nanostructures for use in TCE.

Keyword : Plasma, Dewetting, Nanoparticle Array, Organic Solar Cell, Photocatalysis, Surface Plasmon

Student Number : 2010 – 20641

# Table of Contents

|  |    |
|--|----|
| Abstract.....                                | 1  |
| Table of Contents.....                       | 4  |
| List of Tables.....                          | 6  |
| List of Figures.....                         | 7  |
| I. INTRODUCTION.....                         | 11 |
| 1.1 Plasma-induced Dewetting.....            | 11 |
| 1.2 Applications.....                        | 14 |
| 1.2.1 Organic Solar Cells.....               | 14 |
| 1.2.2 Photocatalytic Activity.....           | 15 |
| 1.2.3 Transparent Conductive Electrodes..... | 16 |
| 1.3 Research background and theory.....      | 19 |
| II. EXPERIMENTAL.....                        | 27 |
| 2.1 Deposition Method.....                   | 27 |
| 2.1.1 Substrate.....                         | 27 |
| 2.1.2 Deposition System.....                 | 27 |
| 2.1.3 Deposition Process.....                | 28 |
| 2.2 Plasma Treatment.....                    | 29 |
| 2.2.1 Plasma Treatment System.....           | 29 |
| 2.2.2 Plasma Treatment Process.....          | 30 |

|  |     |
|--|-----|
| 2.3 Analysis Methods.....                    | 30  |
| 2.3.1 Surface Morphology.....                | 30  |
| 2.3.2 Film Characterization.....             | 31  |
| III. RESULTS AND DISCUSSION.....             | 38  |
| 3.1 Plasma-Induced Dewetting Process.....    | 38  |
| 3.2 Formation of Nanoparticle Array.....     | 53  |
| 3.3 Applications of Nanostructure.....       | 74  |
| 3.3.1 Organic solar cell.....                | 74  |
| 3.3.2 Photocatalytic Activity.....           | 80  |
| 3.3.3 Transparent Conductive Electrodes..... | 85  |
| IV. CONCLUSION.....                          | 91  |
| V. REFERENCES.....                           | 93  |
| VI. 국문초록.....                                | 108 |

# List of Tables

Table. 1-1 Sheet resistance ( $R_s$ ) requirement of various applications.

Table. 2-1 Parameters used during the deposition of the metallic thin films.

Table. 2-2 Parameters used during the inductively coupled  
plasma treatment.

Table. 3-1-1 Root mean square (RMS) average roughness, and the  
maximum height obtained during the dewetting process,  
with increasing plasma treatment time.

Table. 3-2-1 Characteristics of the nanoparticle arrays obtained via  
one-time and two-time dewetting Table. 3-3-1 Photovoltaic  
characteristics obtained when the size and number of nanoparticles  
in the organic solar cell are varied.

Table. 3-3-2 Transmittance and sheet resistance data from different stages  
of the dewetting process of DC- and ICP-sputter-deposited  
6- and 8-nm-thick Au films.

# List of Figures

Fig. 1-1 Schematic of the thin film dewetting.

Fig. 2-1 Schematic of the ICP sputtering system.

Fig. 2-2 Schematic of the plasma treatment chamber.

Fig. 2-3 Temperature of the plasma treatment chamber as function of the time.

Fig. 3-1-1 FE-SEM images obtained at different stages of the dewetting process of 3.1-nm-thick Au films that were subjected to a plasma treatment for (a) 10 s (b) 15 s (c) 20 s (d) 40 s.

Fig. 3-1-2 FE-SEM images obtained at different stages of the dewetting process of 4.5-nm-thick Au films that were plasma-treated for (a) 15 s (b) 20 s (c) 40 s (d) 80 s.

Fig. 3-1-3 FE-SEM images obtained at different stages of the dewetting process of 6.2-nm-thick Au films that were plasma-treated for (a) 20 s (b) 40 s (c) 80 s (d) 120 s.

Fig. 3-1-4 FE-SEM images obtained, at a magnification of 10,000, showing the completion of large-scale dewetting of the 3.1-nm, 4.5-nm, and 6.2-nm-thick Au films.

Fig. 3-1-5 Normalized open area as a function of plasma treatment time of films with differing thicknesses.

Fig. 3-1-6 Tilt-view AFM images of the 6.2-nm-thick Au films that were plasma-treated for (a) 10 s (b) 20 s (c) 40 s (d) 80 s.

Fig. 3-1-7 Top-view AFM images of the 6.2-nm-thick Au films that were plasma-treated for (a) 10 s (b) 20 s (c) 40 s (d) 80 s; the scale bar represents 100 nm in all cases.

Fig. 3-1-8 Grazing-incidence small-angle X-ray scattering (GISAXS) spectra of the Au (111) peak during the plasma-induced dewetting process.

Fig. 3-1-9 Reciprocal number of the full width half maximum, of the XRD data shown in Fig. 3-1-8, as a function of the root value of the plasma treatment time.

Fig. 3-1-10 Dependence of the crystallite size, as determined by using the Debye-Scherrer formula, on the plasma treatment time.

Fig. 3-2-1 Absolute value of the real part of the dielectric function, of various metals, as a function of the wavelength.

Fig. 3-2-2 Imaginary part of the dielectric function, of various metals, as a function of the wavelength.

Fig. 3-2-3 Quality factor, of various metals, as a function of the wavelength.

Fig. 3-2-4 Top-view FE-SEM images of 3.1-nm, 4.5-nm, and 6.2-nm-thick Au films subjected to a H<sub>2</sub> plasma treatment; the images were obtained at magnification of 50,000 $\times$ .

Fig. 3-2-5 Top-view FE-SEM images of 9.3-nm, 12.4-nm, and 15.5-nm-thick Au films subjected to a H<sub>2</sub> plasma treatment; the images were obtained at magnification of 20,000 $\times$ .

Fig. 3-2-6 FE-SEM images of Ag and Cu films subjected to a H<sub>2</sub> plasma treatment; images were obtained at a magnification of 50,000.

Fig. 3-2-7 Dependence of the average diameter of the nanoparticle array on the average thickness of the Au film.

Fig. 3-2-8 Density of the Au film (as determined via X-ray reflectometry and Rutherford backscattering spectrometry) as a function of the ICP power.

Fig. 3-2-9 Cumulative number of particle sizes of plasma-treated Au films that had differing initial densities.

Fig. 3-2-10 Size distribution of nanoparticles formed during the dewetting of films with differing thickness and density.

Fig. 3-2-11 FE-SEM images showing films with different initial thicknesses; these films were subjected to a plasma pre-treatment for various times, prior to a plasma treatment at 700 W for 15 min.

Fig. 3-2-12 FE-SEM images showing various nanoparticle arrays obtained through a repeated dewetting process that consists of two deposition steps and a plasma treatment.

Fig. 3-2-13 FE-SEM images of nanoparticle arrays obtained via deposition on, and plasma dewetting of, a pre-existing bi-continuous structure.

Fig. 3-3-1 Schematic of organic solar cell structure showing the Au nanoparticles deposited on the ITO, in order to enhance the efficiency via the near-field effect.

Fig. 3-3-2 Current density-voltage (J-V) curves obtained when the size and number of nanoparticles in the organic solar cell are varied.

Fig. 3-3-3 FE-SEM images of (a) TiO<sub>2</sub> on quartz, (b) 27-nm Au-nanoparticle array on TiO<sub>2</sub> and (c) 43-nm Au-nanoparticle array.

Fig. 3-3-4 UV spectra collected after 2 h UV-Vis illumination of a methylene blue solution associated with various TiO<sub>2</sub> and Au-nanoparticle samples.

Fig. 3-3-5 A reaction mechanism of Au-TiO<sub>2</sub> for the degradation of azo dyes under UV light irradiation [96].

Fig. 3-3-6 A reaction mechanism of Au-TiO<sub>2</sub> for the degradation of azo dyes under visible light irradiation [96]. obtained via the plasma treatment of films with various initial thicknesses. The open area, i.e., region of the substrate that is exposed, ranges from 30–70%.

Fig. 3-3-8 Dependence of the sheet resistance and transmittance on the thickness of the Au film deposited on quartz.

# I. INTRODUCTION

## 1.1 Plasma-induced dewetting

Metal-nanoparticle arrays are used in various applications such as solar cells [1–5], surface enhanced Raman scattering (SERS) [6], catalysts for nanowire growth [7,8], antibacterial activity [9], and photocatalytic decomposition [10], etc.

Various methods have been used to fabricate these arrays. For example, chemical synthesis is widely used for the fabrication of relatively uniformly sized and size-controllable nanoparticles. However, the toxicity and flammability of the chemicals used, particle agglomeration, and poor dispersion constitute major drawbacks of this method [11,12]. Another method, electron beam lithography yields high-density high-aspect-ratio nanoparticles, but includes multiple processes, requires expensive equipment, and is characterized by a low throughput [13]. X-ray, ultraviolet (UV) lithography, scanning probe lithography, and nanotransfer molding are also used to fabricate nanoparticle arrays [14–23].

Owing to the low processing costs, and simple process that can be performed over large areas, solid-state dewetting constitutes one of the

most promising methods for the fabrication of these arrays. This process is performed without the use of organic materials and hence, the resulting nanoparticles are not contaminated by an organic solution.

Solid-state dewetting, a physical phenomenon, results in the disintegration of thin films into a set of droplets or particles. This process is driven by surface energy minimization and the interfacial energy of the film on the substrate. In addition, this process occurs at temperatures below the melting temperature of the metallic films via diffusion in the solid state [24].

Dewetting is initiated by hole formation which occurs via grain boundary triple junctions [25], thermal grooving at the grain boundary [26], and nucleation by voids at the interface of the film and substrate [27]. These holes then grow by means of a retracting edge, rim pinch off, and fingering instability [25], etc. During the process, the thin metallic film is transformed to a bi-continuous film and finally, to an array of nanoparticles.

Dewetting can be achieved via thermal annealing, pulsed laser [23,28,29], ion beam [30], and electron beam [31] methods. Thermal annealing is a simple and low-cost process and is therefore widely used. However, the low uniformity of the resulting nanoparticles compared to that of other dewetting methods, and long processing time represent major drawbacks of this method. Dewetting by pulsed laser, ion beam, and electron beam yields highly uniform nanoparticle arrays but have a low

throughput and must be performed at high temperatures.

Plasma-induced dewetting offers several advantages compared to thermal annealing. For example, the former must be performed at temperatures higher than ~600 K in order to achieve complete solid-state dewetting, whereas the latter is a low-temperature process. Polymers such as polycarbonate (PC), polyimide (PI), polyethersulfone (PES) can be used as substrates during this process. In addition, the time required for complete dewetting is shorter than those of other methods. Oxidation of the nanoparticles is therefore minimized owing to this short processing time and low processing temperature.

Plasma-induced dewetting yields arrays that have highly uniform nanoparticle sizes. Controllability of the nanoparticle size is essential for adjusting the wavelength at which surface plasmon resonance occurs. Moreover, the process can be performed over large-scale areas and hence mass production of the nanoparticle arrays is possible.

In this study, a high-density plasma is discharged by using an external inductively coupled plasma (ICP) system. The RF power and plasma treatment time are varied and the optimum condition for fabricating the nanostructure is determined. With this method, damage-free use of various substrates (Si, SiO<sub>2</sub>, quartz, ITO, PC, PES, and PI) and sufficient reproducibility of the nanoparticle size and uniformity over the entire

substrate area, were realized.

## 1.2 Applications

The nanoparticle array and bi-continuous nano-film fabricated via plasma-induced dewetting were used for organic solar cells, photocatalytic activity, and transparent conductive electrode materials.

### 1.2.1 Organic solar cells

The incorporation of novel metal-nanoparticle arrays has typically been used to improve the performance of solar cells via the plasmon-enhanced absorption effect [33–34]. The array may be incorporated into the active layer, within the PE-DOT:PSS, between the PEDOT:PSS and anode, as well as between the active and electron transport layers of the cell [1,2,4,35–39]. In this study, a Au-metal nanoparticle array was fabricated on indium tin oxide (ITO) surfaces by using plasma-induced dewetting to produce localized surface plasmons. This method is quite applicable to organic solar cells, from the viewpoint of nanoparticle size control and uniformity over the entire cell, with minimum damage to the ITO substrate or other layers. The size of the Au nanoparticles was varied in order to

achieve an overlap of the active layer absorption band and the Au-nanoparticle plasmonic resonance frequency. An optimum size was suggested, in order to maximize the power conversion efficiency via the near-field effect.

### 1.2.2 Photocatalytic Activity

Photocatalytic decomposition of organic molecules, with the aim of removing pollutants, has been extensively studied. Titanium dioxide ( $\text{TiO}_2$ ) is non-toxic, relatively cheap, and exhibits excellent photostability over a wide PH range as well as under UV light irradiation [40–47];  $\text{TiO}_2$  constitutes therefore one of the typical semiconductor materials ( $\text{TiO}_2$ ,  $\text{ZnO}$ ,  $\text{SnO}$ ,  $\text{In}_2\text{O}_3$ ) that are used as heterogeneous photocatalysts. In fact, owing to its photocatalytic properties, anatase  $\text{TiO}_2$  has been used in the degradation of toxic dyes and environmental pollutants [48,49].  $\text{TiO}_2$  has, however, limited optical properties, as manifested by a band gap energy of 3.2 eV (which lies within the UV-light region only) and rapid recombination of photo-generated electron-hole pairs [50]. UV light constitutes only 3–5% of the entire solar spectrum and therefore, various methods have been developed in order to extend the optical spectrum of  $\text{TiO}_2$  to the visible range [10,43,51–55]. Noble metal nanoparticles have received attention in

this regard; Au has received particular attention owing to its photostability and plasmonic properties, which produce intense electric-field amplitudes through excitation of the localized surface plasmon resonance [56–59].

As such, in this study, a Au-nanoparticle array was deposited on TiO<sub>2</sub> in order to improve the photocatalytic efficiency of the system. Plasma-induced dewetting of Au films was conducted successfully without damage to, or deformation of, the TiO<sub>2</sub> substrates by using an optimized plasma treatment time. The photocatalytic activity of TiO<sub>2</sub> was evaluated by examining the photo-degradation of methylene blue (MB) under UV or visible light irradiation.

### 1.2.3 Transparent conductive electrodes

Transparent conductive electrodes (TCE) are essential for providing electrical contact with the active layer and the transmission of light with minimum loss in the display device and solar cells [60–63]. The well-known material, ITO, has outstanding properties, which are excellent electrical and optical performance for application of TCE. The price of ITO has, however, steadily increased owing to the low abundance limit of indium and increasing demand for ITO. In addition, thin films of ITO are typically brittle and have low infrared transmittance [64]. Alternatives to ITO

including carbon nanotubes (CNT) and graphene [65–74], conducting polymers [64], and metal nanowire-based electrodes [75–83], have therefore been extensively investigated. Among these candidates, noble metal-based-structure TCE have received particular attention owing to their high conductivity, which is characteristic of noble metals. The sheet resistance ( $R_s$ ) and optical transmittance (T) play a key role in the performance of TCE. Table. 1-1 shows the  $R_s$  requirement of various applications [73].

A Au bi-continuous film on a transparent substrate, fabricated by using a proper plasma treatment time, has significant potential for use in TCE. When a general plasma treatment time was used for dewetting, the Au nano-film fragmented into a spherical nanoparticle array and the sheet resistance increased infinitely. However, if the optimum process conditions were applied to a fully interconnected bi-continuous film, then tunable sheet resistance and optical transmittance that fell within the range required for TCE application, were obtained. In this study, the thickness of the Au film and the plasma treatment time were varied in order to realize conductivity and a bi-continuous structure, respectively, that satisfied the TCE requirements. In this regard, the plasma-induced dewetting method is deemed a simple, fast, and efficient process for fabricating continuous metal nanostructures for TCE.

| Transparent Electrode Type | Device Type                      | $R_s$ Range<br>( $\Omega$ /sq.) |
|----------------------------|----------------------------------|---------------------------------|
| Touch side                 | Resistive touch panel            | 300 – 500                       |
| Device side                | Resistive touch panel            | 200 – 500                       |
| Top and Bottom             | Projected Capacitive touch panel | 100 – 300                       |
| Primary                    | Surface Capacitive touch panel   | 900 – 1500                      |
| Pixel                      | LCD                              | 100 – 300                       |
| Common                     | LCD                              | 30 – 80                         |

Table. 1-1 Sheet resistance ( $R_s$ ) requirement of various applications [73].

## 1.3 Research background and theory

### 1.3.1. Dewetting of thin films

Dewetting of a thin film may occur in the case of a liquid film deposited on either a solid or liquid substrate. This process refers to the rupture of the film on the substrate and the consequent formation of droplets as shown in Fig. 1-1. The rupture is driven by minimization of the total energy of the free surface of the film and substrate. This minimization is typically expressed in terms of the change in the Gibbs energy,  $\Delta G$ .

Owing to the simplicity of the model system of a thin (<60 nm) liquid film on a solid substrate, the effective interface potential,  $G(h)$  may be determined;  $h$  is the film thickness [84, 85]. With knowledge of  $G(h)$ , three states of the film, stable, unstable, and metastable, may be considered.

In unstable regions, the film may be ruptured via heterogeneous nucleation, thermal nucleation, and spinodal dewetting. In heterogeneous nucleation, holes are nucleated at defects on the film surface. Thermal (hole) nucleation occurs if thermal activation is sufficient to overcome the potential barrier for nucleation of a defect [86]. Spinodal dewetting can be described mathematically. In the case of very thin (<60 nm) films, the fluctuations in the two surfaces become correlated owing to the molecular

interactions in the film. Van der Waals forces are always present and tend to drive the molecules from the thinner to the thicker parts of the film.

However, the surface tension has the opposite effect and results, in general, in a flattening of the film surface. The increase in the Gibbs energy of the surface will therefore be compensated by the total decrease in the Van der Waals energy.

Consider a 1 nm (length)  $\times$   $\Lambda$  cm (width) region of the film, whose deformation constitutes one of the many Fourier components that comprise the total perturbation of the film. The Gibbs energy,  $\Delta G$ , contained in this particular wave, compared to a completely flat film of thickness,  $h_0$ , can be expressed as:

$$\Delta G = \text{extra area} \times \gamma + \text{extra interaction energy}$$

Where  $\gamma$  is the surface tension. The extra area on both sides of the film is given by:

$$2 \int_{y=0}^{y=\Lambda} \sqrt{(dz)^2 + (dy)^2} - dy = 2 \int_0^\Lambda \sqrt{1 + \left(\frac{dz}{dy}\right)^2} - 1 \, dy = \int_0^\Lambda \left(\frac{dz}{dy}\right)^2 \, dy$$

If  $G(h)$  is the Gibbs energy of interaction per unit area among all of the molecules in the film, then the extra interaction energy in the wave form

is given by:

$$\int_0^\Lambda \frac{dG(h)}{dh} \Delta h + \frac{1}{2} \frac{d^2G(h)}{dh^2} (\Delta h)^2 dy$$

$$\Delta G = \gamma \int_0^\Lambda \left( \frac{dz}{dy} \right)^2 dy + \int_0^\Lambda \left( \frac{dG}{dh} \right) 2B \sin\left( \frac{2\pi y}{\Lambda} \right) dy + \frac{1}{2} \int_0^\Lambda \frac{d^2G}{dh^2} 4B^2 \left( \sin \frac{2\pi y}{\Lambda} \right)^2 dy$$

$$= \gamma B^2 \frac{4\pi^2}{\Lambda^2} \int_0^\Lambda \left( \cos \frac{2\pi y}{\Lambda} \right)^2 dy + 0 + 2B^2 \frac{d^2G}{dh^2} \int_0^\Lambda \left( \sin \frac{2\pi y}{\Lambda} \right)^2 dy$$

This particular fluctuation will grow, if the total Gibbs energy is negative. The condition for growth is expressed as:

$$\gamma B^2 \frac{4\pi^2}{\Lambda^2} + 2B^2 \frac{d^2G}{dh^2} < 0$$

$$\Lambda > \Lambda_{crit} = \sqrt{-2\pi^2 \gamma / \left( \frac{d^2G}{dh^2} \right)}$$

In most cases, the film is extremely wide (i.e.,  $\Lambda \gg h_0$ ) and therefore, the first term of upper equation can be set to 0. The perturbation of the film grows when  $G''(h) < 0$  and leads eventually, to fragmentation. This dewetting mechanism, which is referred to as spinodal dewetting, is characterized by periodic fluctuations and, therefore yields uniformly distributed nanoparticles.

### 2.1.2 Solid-state dewetting of thin films

In solid-state thin films, the unstable or metastable condition in which dewetting occurs is satisfied by specific substrates and film systems. The corresponding energy minimization is described by the Young-Laplace equation:

$$\gamma_s = \gamma_i + \gamma_f \cos \theta$$

Where  $\gamma_f$ ,  $\gamma_i$ ,  $\gamma_s$ , and  $\theta$  are the surface energy of the nanoparticle, energy of the nanoparticle-substrate interface, surface energy of the substrate, and the equilibrium contact angle, respectively.

When  $\gamma_f + \gamma_i > \gamma_s$ , the film dewets at sufficiently high rates of the relevant kinetic processes. Oxide or polymer materials are used as the substrate in most applications and therefore, almost all metallic films can be dewet. If the dewetting condition is satisfied, then the solid-state thin film is dewet via hole formation and growth.

According to Mullins [87], Planar surfaces with isotropic surface energies are stable with respect to all perturbations whose amplitudes are lower than the film thickness. Consequently, a defect-free film dewets only when a high-amplitude perturbation is applied (homogeneous hole

nucleation mechanism). Flat surfaces are stable with respect to small perturbations, and hence a process that leads to hole formation is required for dewetting at relatively low energies. In the case of a polycrystalline film, grain boundaries and triple junctions play an important role in hole formation. Srolovitz et al. made two assumptions in order to determine the effect of grain boundaries on dewetting. The first is that at equilibrium, the angle between the grain boundary and the free surface is the equilibrium notch angle. The second is that a shape with a circular base and minimum surface area is a spherical cap. Therefore, a sphere (spherical shape) constitutes the minimum surface-energy shape.

The equilibrium contact angle can be expressed as:

$$\theta = \sin^{-1} \left( \frac{\gamma_{\text{grainboundary}}}{2\gamma_f} \right)$$

Assuming conservation of film volume, then the equilibrium groove depth,  $d$ , is given as:

$$d = R \frac{2 - 3\cos\theta + \cos^3\theta}{3\sin^3\theta}$$

This grain boundary groove reaches a finite depth even after an

infinite time process, such as annealing. Therefore, the conditions under which the groove intercepts the substrate may be determined. A thin film will rupture if:

$$\frac{R}{a} \geq \frac{3 \sin^3 \theta}{2 - 3 \cos \theta + \cos^3 \theta}$$

Grain boundaries satisfying this condition can therefore act as hole nucleation sites.

In fact, hole nucleation will most likely occur at high-energy grain boundaries, small  $\gamma_f$  and  $h$  conditions, and large  $\gamma_{gb}$  and  $R$  conditions. Moreover, owing to the finite processing time, sufficient energy must be transferred to the film during the process even if the surface energy and angle at the grain boundaries satisfy the dewetting condition.

Srolovitz et al. also showed that holes were most likely nucleated at grain boundary triple junctions first. In addition, during heterogeneous hole nucleation, other surface defects can act as hole nucleation sites. As previously mentioned, however, homogeneous hole nucleation may be induced at high energies.

After hole formation, capillary energy drives the retraction of the hole edge and the hole grows. This growth occurs primarily via diffusion. During thermal annealing, the dewetted areas that grow from the holes are

sparse and separated by distances greater than the grain size. This is consistent with studies, which showed that holes are only nucleated at some grain boundaries and the growth rate of these holes varies with the grain boundary energy.

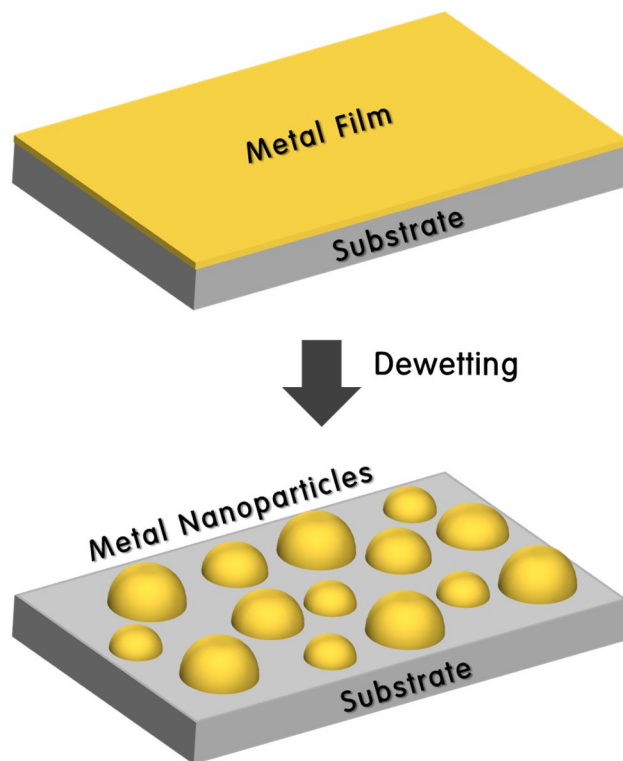


Fig. 1-1 Schematic of the thin film dewetting.

## II. EXPERIMENTAL

### 2.1 Deposition method

#### 2.1.1 Substrate

Silicon was the main substrate used to investigate the mechanism of solid-state dewetting by means of a plasma treatment. Quartz, ITO, and amorphous SiO<sub>2</sub> were used for conductive transparent metallic films, solar cells, and TiO<sub>2</sub> photocatalytic experiments, respectively. Samples with a maximum size of 35 mm × 50 mm were investigated.

#### 2.1.2 Deposition system

Metallic films of Au, Ag, and Cu were deposited via ICP-assisted reactive magnetron sputtering. An all-metal target (>99.995%, diameter: 7.62 cm) was used as the sputtering target and the film was deposited under an Ar atmosphere. A schematic of the ICP sputtering system is shown in Fig. 1. The sputter gun was operated by DC power sources. A 135-mm-diameter two-turn copper coil, shielded by an insulating material,

was placed between the target and the substrate in the cylindrical stainless steel chamber. The ICP was generated by applying an RF power (13.56 MHz) through a tuning network to the coil, using an L-type matching network. The chamber was evacuated down to  $\sim 1 \times 10^{-6}$  Torr using a turbo molecular pump, and a butterfly valve was used to set the operating pressure to 10–20 mTorr of Ar gas. The substrate was inserted into the chamber holder, by means of a load-lock system, and electrically connected to DC bias power.

### 2.1.3 Deposition process

The parameters used during the deposition process are listed in Table 1. Prior to the deposition, the substrate was cleaned for 15 min in acetone and ethanol, respectively, in an ultrasonic cleaner, and then blow-dried with nitrogen gas. Where necessary, the substrate was pre-treated, under an Ar atmosphere, by ICP at an RF power of 100 W and a substrate bias voltage of 5–20 V. This pretreatment was performed in order to change the interfacial energy between the substrate and the films.

## 2.2 Plasma Treatment

### 2.2.1 Plasma treatment system

The sputter-deposited films were treated by an external ICP. Fig. 2 shows a schematic of the equipment used to perform the plasma treatment. The base pressure was evacuated to lower than  $3 \times 10^{-7}$  Torr, by using a turbo molecular pump and the operating pressure was raised to 20 mTorr of H<sub>2</sub> gas, by using the controlling butterfly valve. The sample holder was then inserted by using a load-lock system; additional heat was not applied to the samples during the plasma treatment. The RF power was coupled to the external antenna at 13.56 MHz for ICP. An antenna-fabricated three-turn Cu coil was installed on a quartz dielectric plate at the top of the chamber. The sample holder was placed ~150 mm away from the coil. In addition, the temperature of the chamber was measured by a thermocouple located just below the sample holder. The saturation temperature of the plasma treatment chamber was ~544 K, as shown in Fig. 3.

## 2.2.2 Plasma treatment process

The parameters used for the plasma treatment are listed in Table 2. Prior to the treatment, the chamber was cleaned by H<sub>2</sub> plasma at the same operating condition, because the dewetting process may be affected by the pre-existing oxygen in the chamber.

## 2.3 Analysis methods

### 2.3.1 Surface morphology

The surface morphology was examined and cross-sectional images of the films were obtained via field-emission scanning electron microscopy (FE-SEM / JEOL JSM6330F, Hitachi SU70) performed at an acceleration voltage of 5 keV. Furthermore, the coverage of the films was determined from these images, by using the Image-Pro Plus program, to perform a statistical analysis of the metal nanoparticle arrays. A cross-sectional image was obtained and the film thickness was measured by using a focused ion beam (FIB / Carl Zeiss AURIGA). In addition, an atomic force microscope (AFM / NANOSTATION II), having a tip size of ~10 nm, was used to

determine the average roughness of the as-deposited, bi-continuous, dewetted samples. A  $1 \times 1 \mu\text{m}^2$  region of each sample was analyzed, at a topographic resolution of 2 nm.

### 2.3.2 Film characterization

Grazing-incidence small-angle X-ray scattering (GISAXS / Bruker New D8 Advance) was performed on  $10 \times 10 \text{ mm}^2$  samples in order to identify the crystallographic changes that occur during the dewetting process. Scans were performed at a step size of  $0.04^\circ$ , over a scan range of  $37\text{--}39^\circ$ . The crystallite size  $L$  was calculated by using the Debye-Scherrer formula (Eq. 2);  $\beta$ ,  $\lambda$ , and  $\Theta$  are the parameter that accounts for band broadening (and whose value is determined by subtracting the instrumental line broadening from the full width half maximum (FWHM), wavelength ( $1.5418 \text{ \AA}$ )) of Cu  $K_\alpha$  X-rays, and the peak position angle, respectively.

$$L = \frac{K\lambda}{\beta \cos\theta} \quad (\text{Eq. 2})$$

In addition, the density and thickness of the metallic films were measured via X-ray reflectometry (XRR / PANalytical X'pert Pro).

The density of the films was also determined by Rutherford backscattering spectrometry (RBS / NEC 6SDH), in order to increase the reliability of the results. During the measurements, He<sup>+</sup> ions were bombarded at an angle of 9° to the surface normal and the backscattered ions were detected at an angle of 170° to the beam direction.

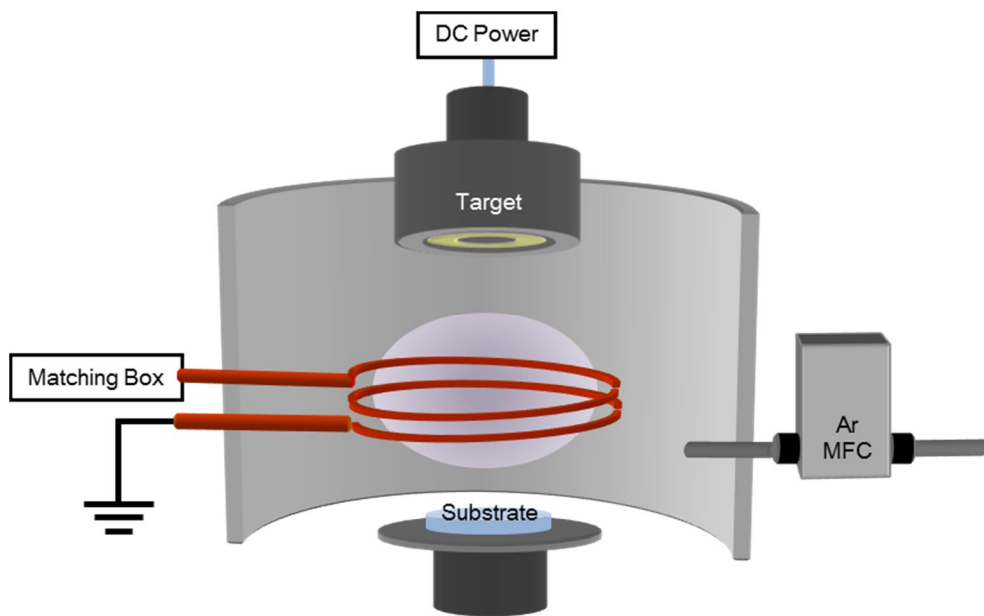


Fig. 2-1 Schematic of the ICP sputtering system.

---

|  |          |
|--|----------|
| Target DC Power / W                    | 70 – 200 |
| ICP RF Power / W                       | 100      |
| Operating pressure / mTorr             | 10–20    |
| Ar flow rate / sccm                    | 20       |
| Substrate bias / V                     | 0 – 20   |
| Deposition rate / nm min <sup>-1</sup> | 4–13     |
| Sample holder size / mm                | 35 × 50  |

---

Table. 2-1 Parameters used during the deposition of the metallic thin films.

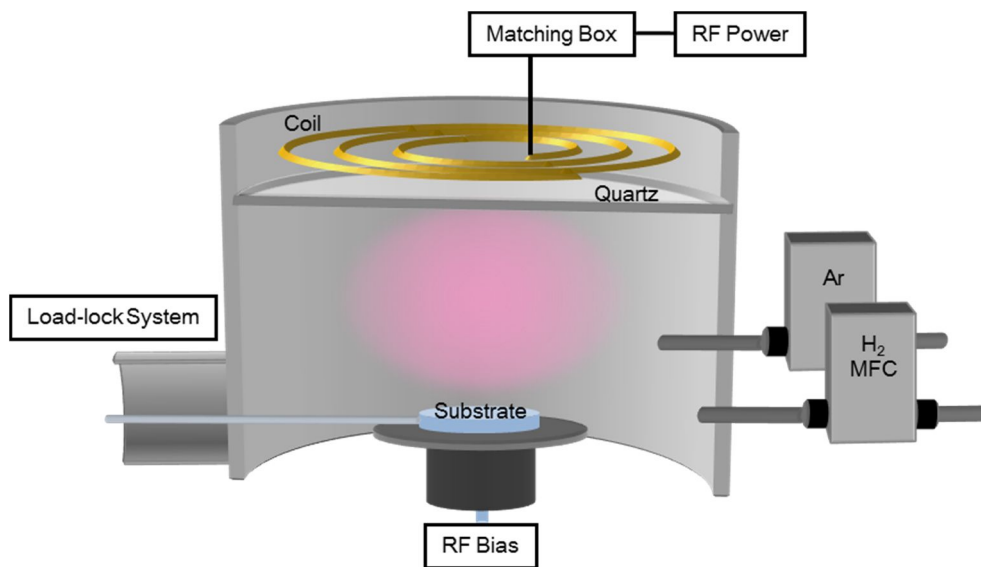


Fig. 2-2 Schematic of the plasma treatment chamber.

---

|                                 |                             |
|---------------------------------|-----------------------------|
| ICP RF Power / W                | 700                         |
| Operating pressure / mTorr      | 20                          |
| H <sub>2</sub> flow rate / sccm | 20                          |
| Substrate bias / V              | 0                           |
| Sample holder size / mm         | 32 × 70                     |
| Chamber cleaning                | Same as operating condition |

---

Table. 2-2 Parameters used during the inductively coupled plasma treatment.

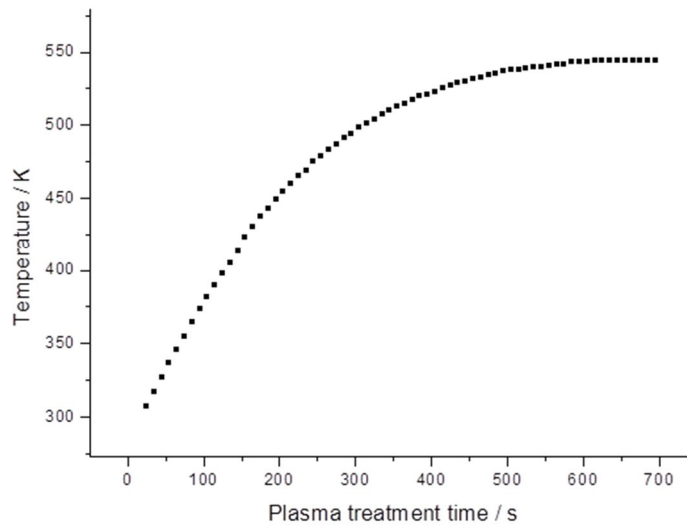


Fig. 2-3 Temperature of the plasma treatment chamber as function of the time.

# III. RESULTS AND DISCUSSION

## 3.1 Plasma-induced dewetting process

A plasma treatment was used for the solid-state dewetting of Au metal films. The plasma-induced dewetting process was investigated by dewetting 3.1-nm, 4.5-nm, and 6.2-nm Au films for various plasma treatment times. This process was initiated with hole nucleation, as shown in Fig. 3-1-1 (a), Fig. 3-1-2 (a), Fig. 3-1-3 (a), at grain boundaries and triple junctions in regions of high local stress or levels of void formation. Hole growth occurs subsequent to nucleation. During solid-state dewetting, hole growth processes such as edge retraction, rim pinch-off, fingering instability occur in the regions surrounding the nucleated holes. Plasma-induced dewetting generates a higher density of holes, and hence hole growth progresses more rapidly, than during other processes. This growth resulted in the formation of a bi-continuous structure, as shown in Fig. 3-1-1 (b), Fig. 3-1-2 (b), and Fig. 3-1-3 (b). In addition, with increasing plasma treatment time, elongated islands fragmented into spherical ones owing to the Rayleigh instability [88,89] and an array of nanoparticles was obtained upon completion of the dewetting process. Dewetting occurred uniformly

over the entire substrate, regardless of the film thickness (Fig. 3-1-4). However, the rate of dewetting decreased with increasing film thickness, thereby resulting in an array consisting of large nanoparticles at the completion of dewetting. The size distribution of the array is considered in detail in section 3.2.

The film coverage ( $c$ ) was determined from FE-SEM images of the dewetted surfaces, by using the Image-pro Plus software to analyze the particles. Fig. 3-1-5 shows the dependence of the normalized open area ( $A_{nor}$ ) on the treatment time.  $A_{nor}$  is calculated from Eq. 2;  $c_s$  is the value of the coverage at saturation. At least 1000 images of the nanoparticles were analyzed.

$$A_{nor} = \frac{1-c}{1-c_s} \quad (\text{Eq. 3})$$

Hole nucleation was delayed and the completion time for dewetting increased, with increasing film thickness. In this work, the completion time of dewetting is defined as the time at which  $A_{nor}$  reaches a value of 95%; based on this definition, the completion times for the 3.1-nm, 4.5-nm, and 6.2-nm-thick Au films are 60 s, 80 s, and 100 s, respectively. These times are significantly shorter than those associated with the other thermal dewetting methods [90–93].

The change in the height and width of a 6.2-nm Au film with increasing plasma treatment time was investigated via atomic force microscopy (AFM); the results are shown in Fig. 3-1-6 and Fig. 3-1-7. As Table. 3-1-1 shows, the root mean square (RMS) average roughness and maximum height increased with increasing plasma treatment time. This resulted from elevation of the rim around the holes (Fig. 3-1-7 (b)) and the gradual fragmentation of elongated islands into spherical particles (Fig. 3-1-7 (c)).

Fig. 3-1-8 shows the GISAXS spectra collected from the Au (111) peak during plasma-induced dewetting of the Au 6.2-nm film. The experiments performed were based on those outlined in the literature [94,95]. The increase in intensity and sharpening of the peak (Fig. 3-1-8) during dewetting are consistent with the changing morphology (Fig. 3-1-3) of the film. The reciprocal number of the full width half maximum (FWHM) of the data shown in Fig. 3-1-8 was plotted (Fig. 3-1-9) as a function of the square root of the plasma treatment time. As the figure shows, this number is linearly proportional to the root value of the processing time. This indicates that Au atoms diffused into the (111) crystalline site during the treatment, thereby resulting in an increase in the size of the (111) grain. Fig. 3-1-10 shows the crystallite size, which was determined by using the Debye-Scherrer formula. Although the size of the crystallites increased with

increasing dewetting time, this size, the XRD curve, and FWHM changed only slightly during dewetting.

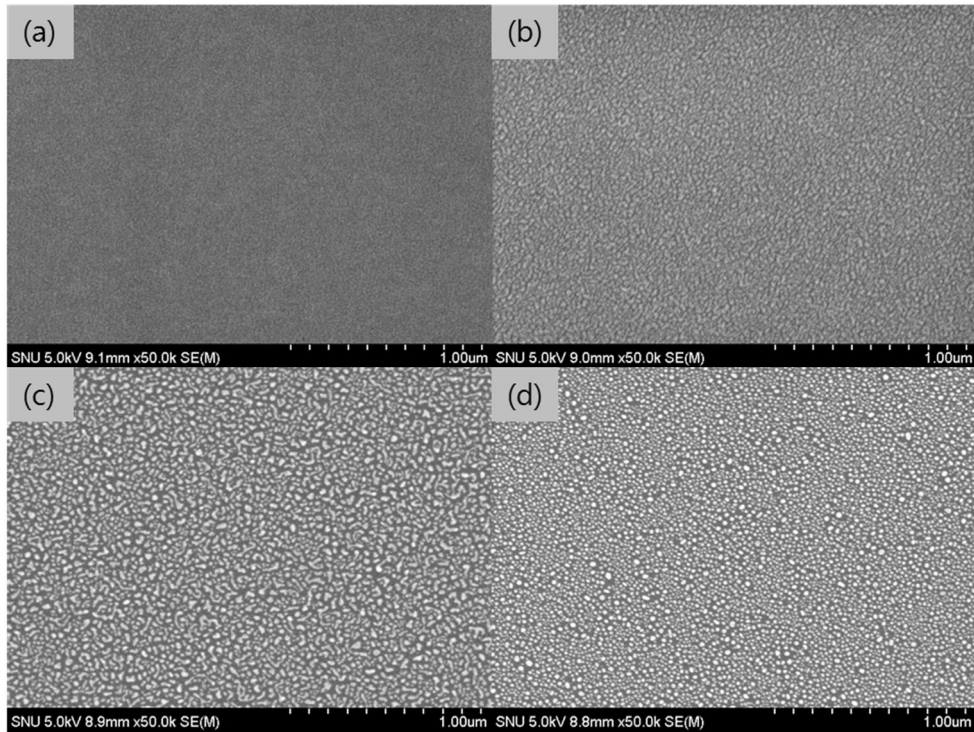


Fig. 3-1-1 FE-SEM images obtained at different stages of the dewetting process of 3.1-nm-thick Au films that were subjected to a plasma treatment for (a) 10 s (b) 15 s (c) 20 s (d) 40 s.

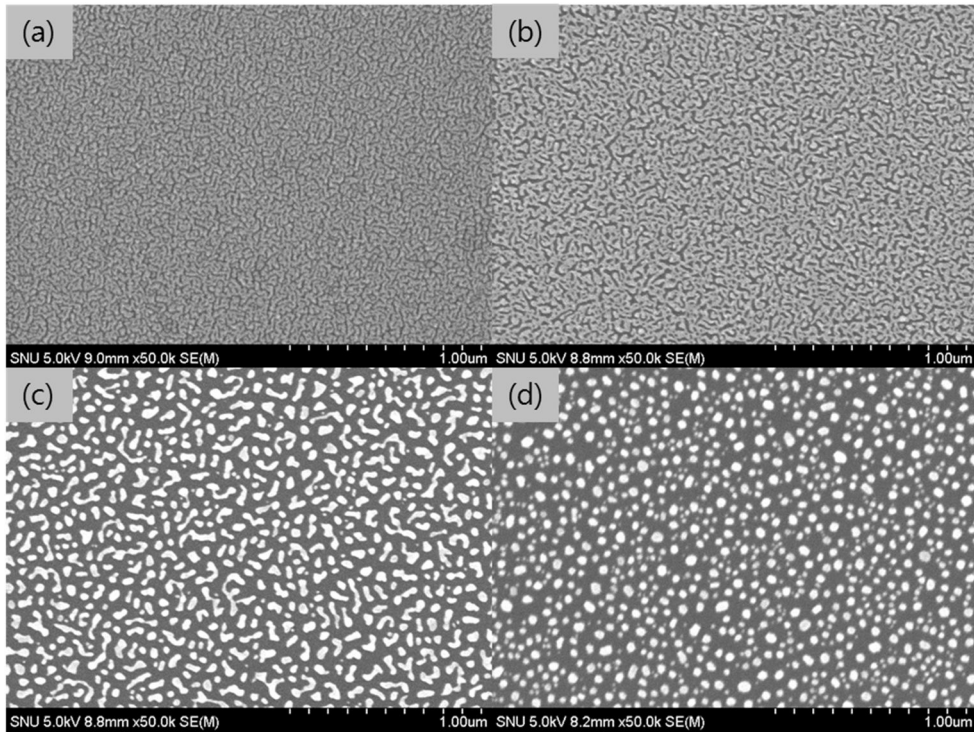


Fig. 3-1-2 FE-SEM images obtained at different stages of the dewetting process of 4.5-nm-thick Au films that were plasma-treated for (a) 15 s (b) 20 s (c) 40 s (d) 80 s.

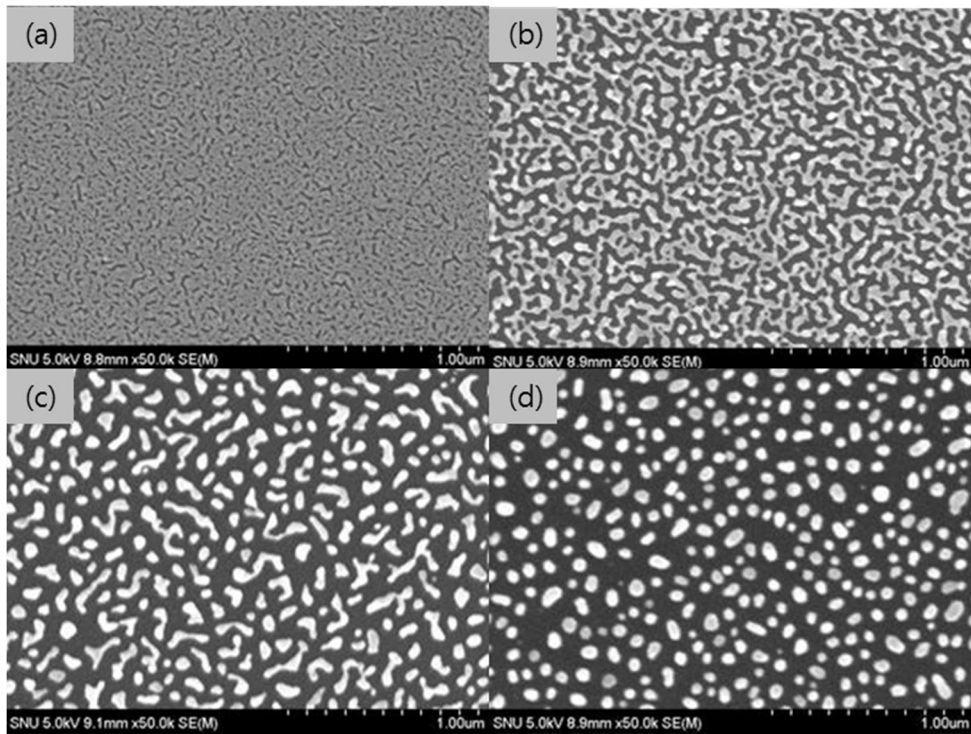


Fig. 3-1-3 FE-SEM images obtained at different stages of the dewetting process of 6.2-nm-thick Au films that were plasma-treated for (a) 20 s (b) 40 s (c) 80 s (d) 120 s.

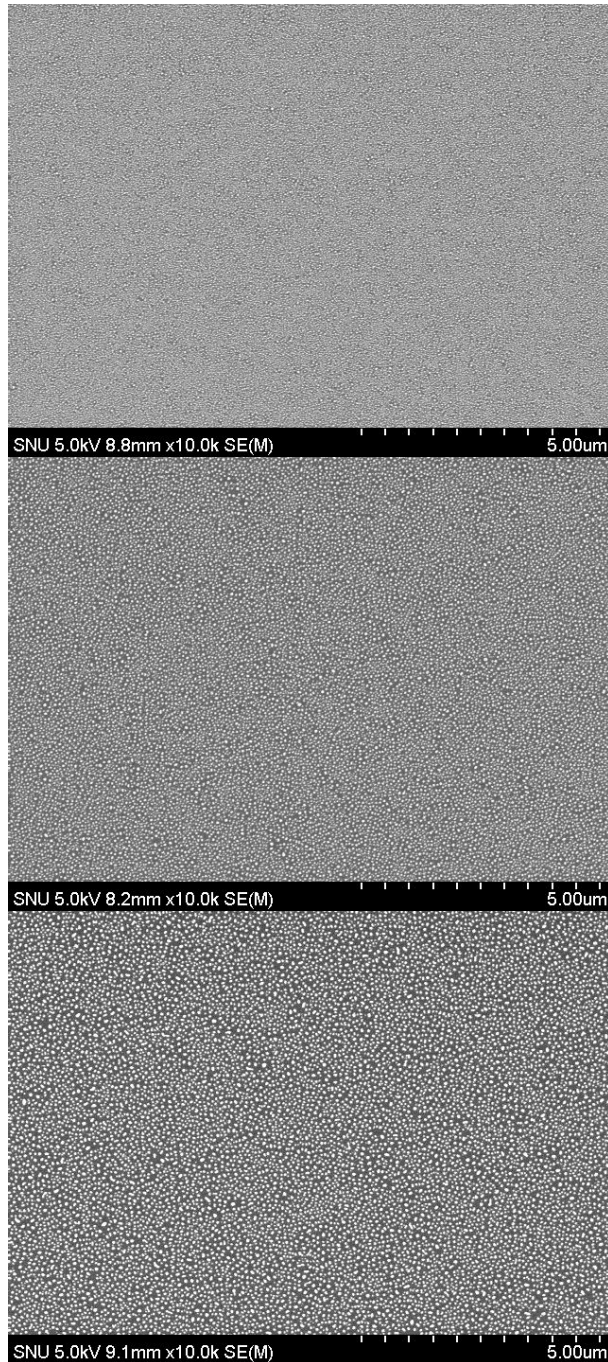


Fig. 3-1-4 FE-SEM images obtained, at a magnification of 10,000, showing the completion of large-scale dewetting of the 3.1-nm, 4.5-nm, and 6.2-nm-thick Au films.

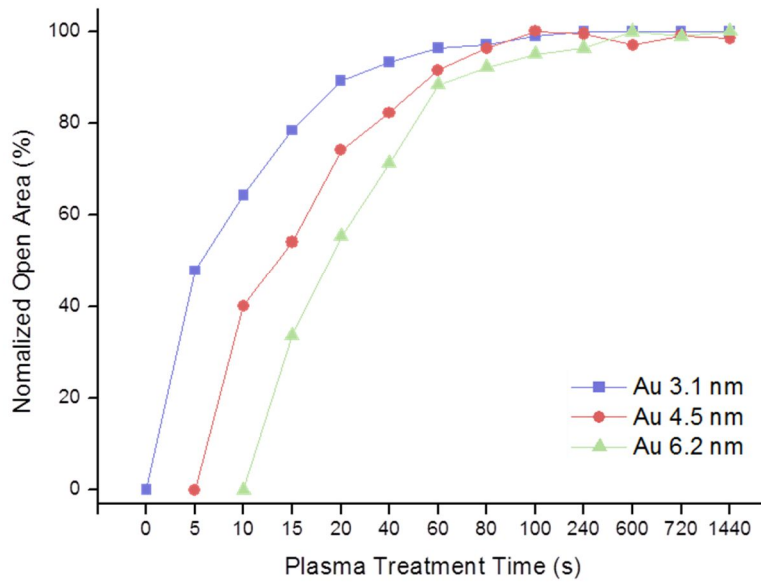


Fig. 3-1-5 Normalized open area as a function of plasma treatment time of films with differing thicknesses.

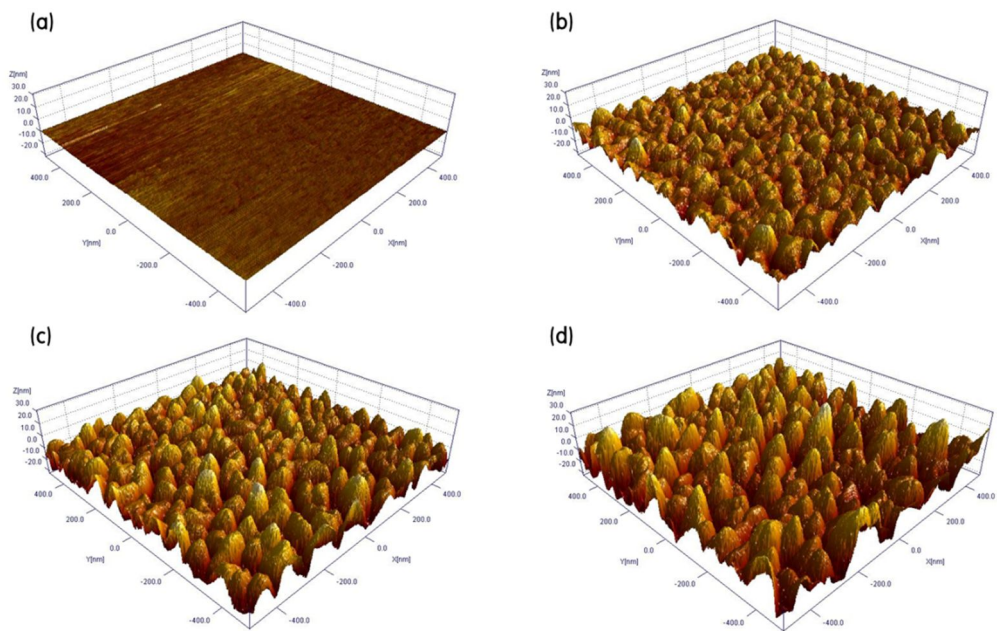


Fig. 3-1-6 Tilt-view AFM images of the 6.2-nm-thick Au films that were plasma-treated for (a) 10 s (b) 20 s (c) 40 s (d) 80 s.

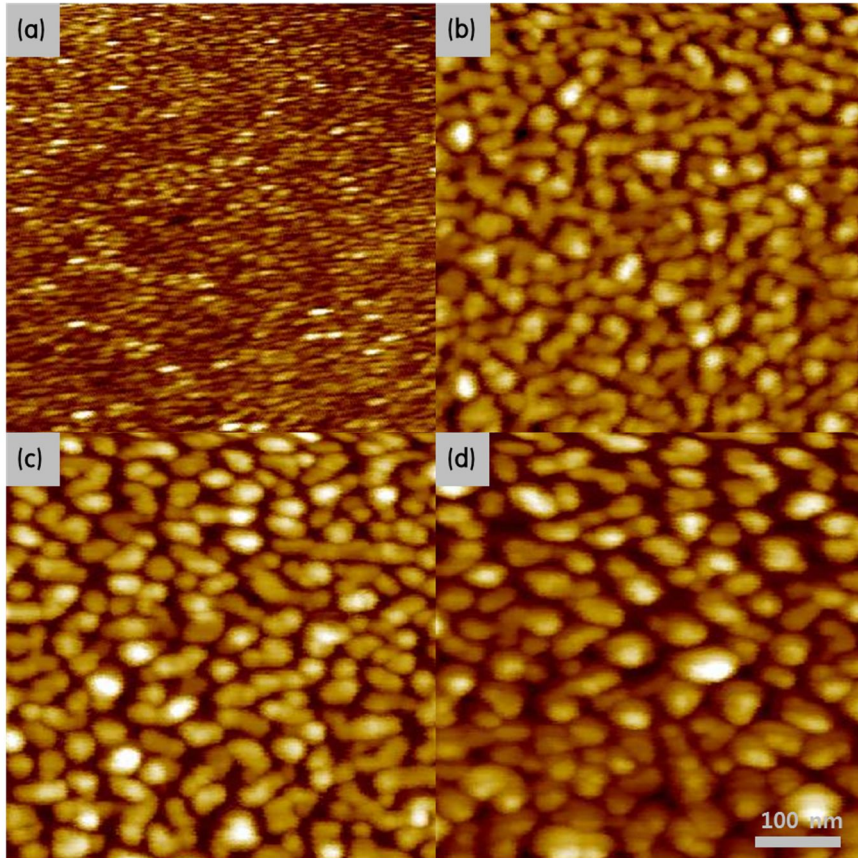


Fig. 3-1-7 Top-view AFM images of the 6.2-nm-thick Au films that were plasma-treated for (a) 10 s (b) 20 s (c) 40 s (d) 80 s; the scale bar represents 100 nm in all cases.

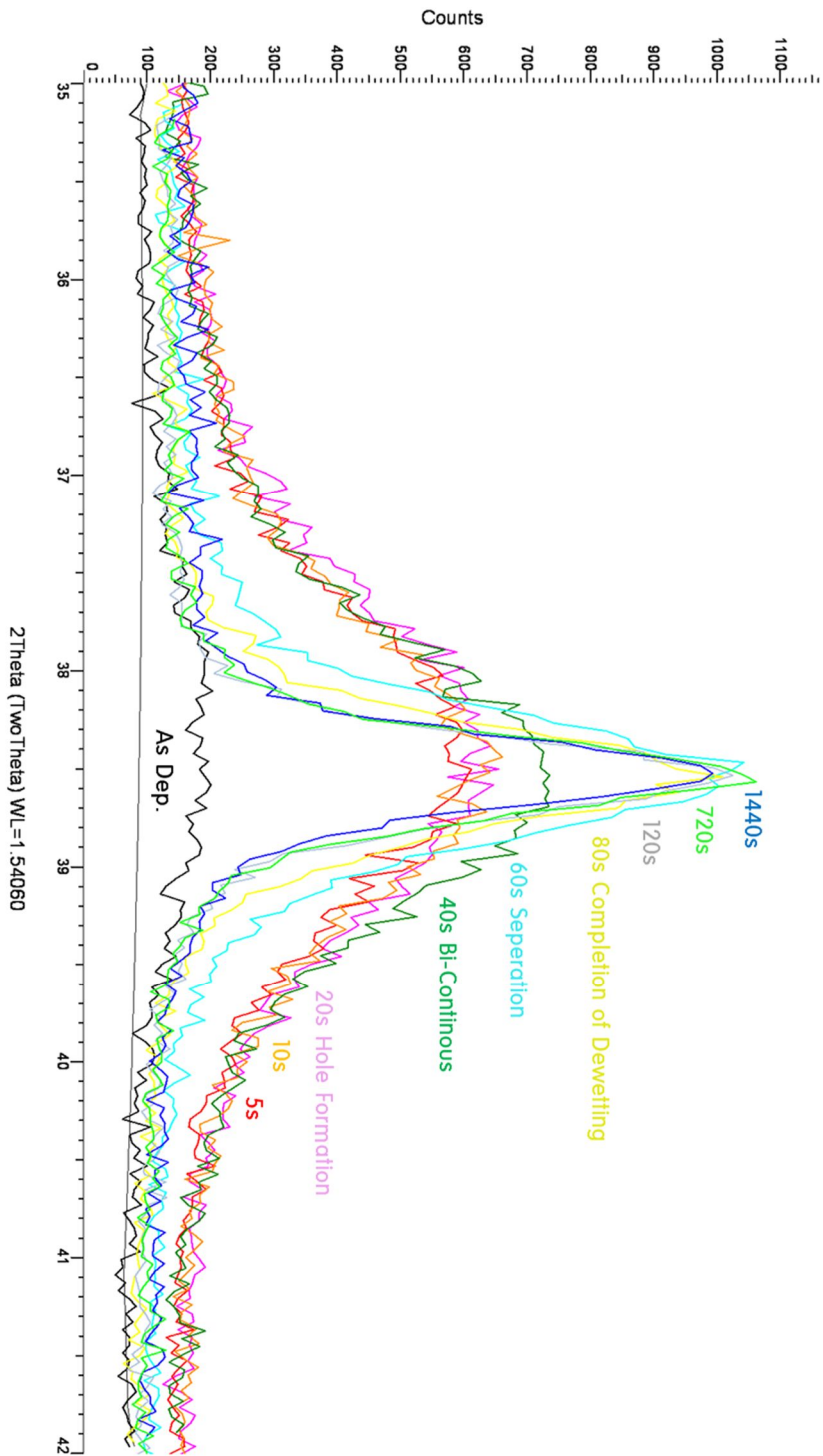


Fig. 3-1-8 Grazing-incidence small-angle X-ray scattering (GISAXS) spectra of the Au (111) peak during the plasma-induced dewetting process.

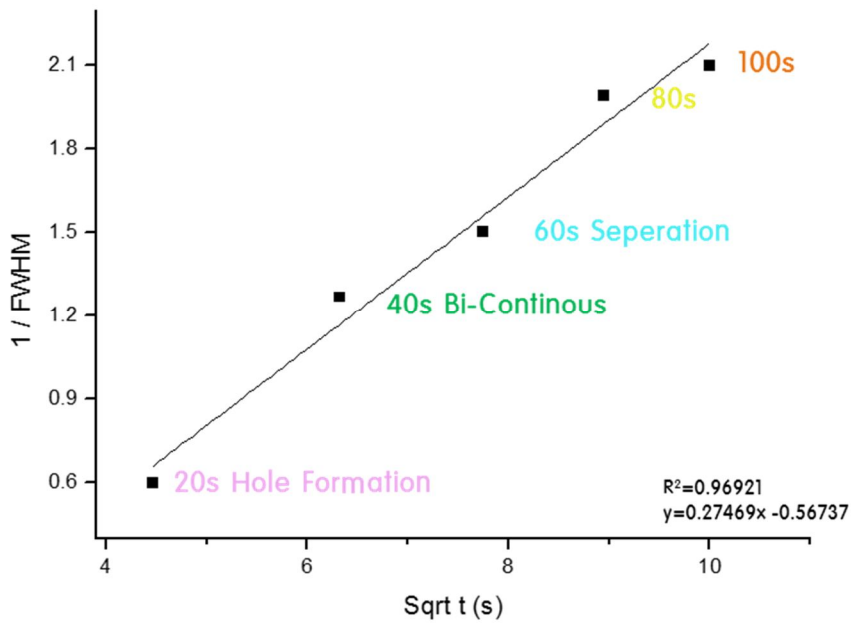
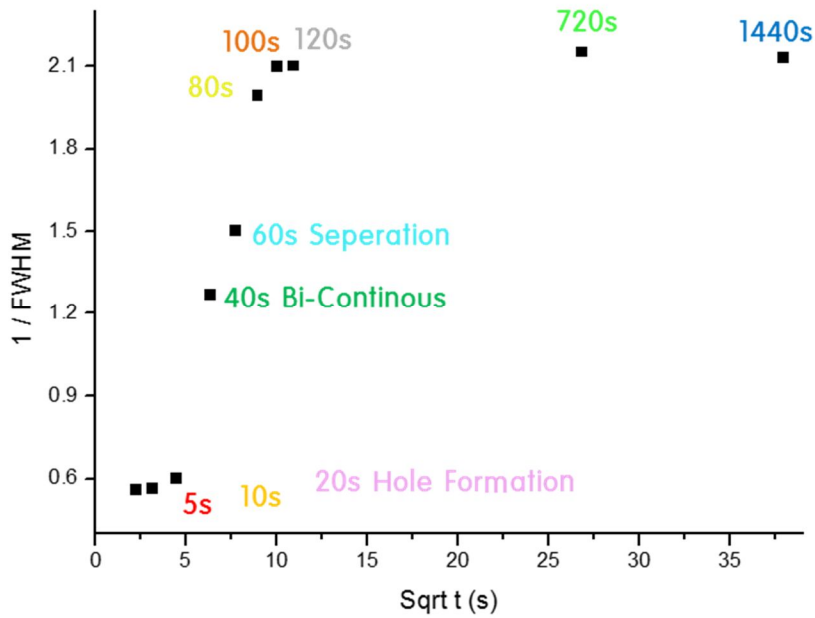


Fig. 3-1-9 Reciprocal number of the full width half maximum, of the XRD data shown in Fig. 3-1-8, as a function of the root value of the plasma treatment time.

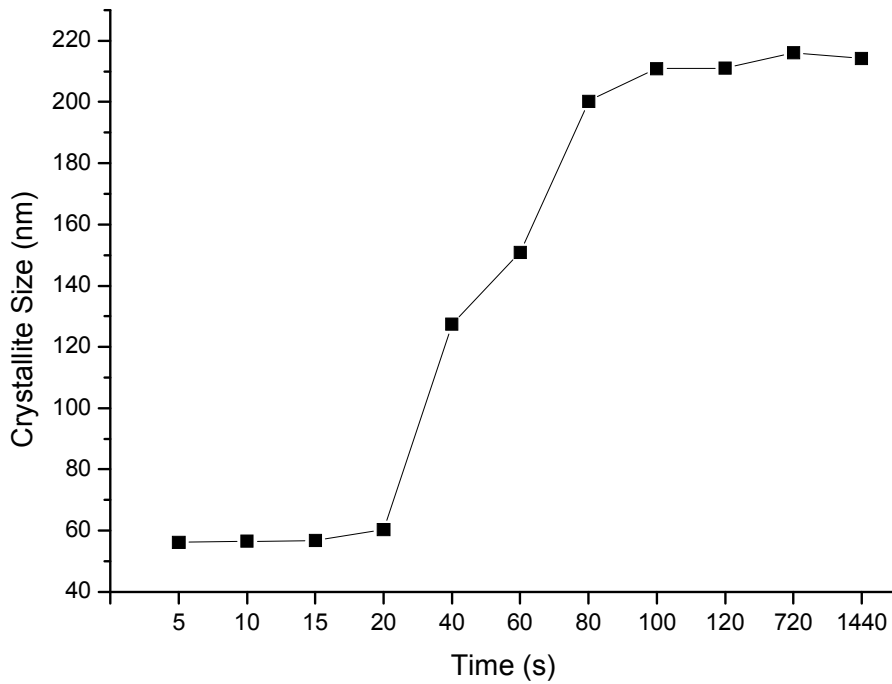


Fig. 3-1-10 Dependence of the crystallite size, as determined by using the Debye-Scherrer formula, on the plasma treatment time.

| Plasma Treatment Time | Average Roughness (RMS) | Max Height |
|-----------------------|-------------------------|------------|
| As-deposited          | 0.27 nm                 | 3.26 nm    |
| 10 s                  | 0.51 nm                 | 4.51 nm    |
| 20 s                  | 3.67 nm                 | 27.1 nm    |
| 40 s                  | 6.37 nm                 | 35.9 nm    |
| 120 s                 | 9.01 nm                 | 52.7 nm    |

Table. 3-1-1 Root mean square (RMS) average roughness, and the maximum height obtained during the dewetting process, with increasing plasma treatment time.

## 3.2 Formation of nanoparticle array

Au, Ag, and Cu thin films were treated by ICP plasma in order to form nanoparticle arrays. These elements, which belong to group 11 of the periodic table, are relatively inert and have low electrical resistivity. In fact, nanoparticles of these materials exhibit strong absorption bands at the ultraviolet-visible wavelengths of light, owing to the plasmon resonance that occurs in that range.

Localized surface plasmon resonance (LSPR), i.e., collective electron charge oscillations, results from an electromagnetic wave induced in the metallic nanoparticles. As the size of nanoparticle change, a specific wavelength of light is required for resonance. The maximum optical absorption occurs at the plasmon resonant frequency. Furthermore, electric fields around the surface of the nanoparticles are enhanced at the resonance wavelength, and this enhancement is significantly reduced with increasing distance from the surface of the nanoparticles. Electromagnetic fields around the nanoparticles can be spatially localized, thereby forming hotspots, via coupling of the plasmonic near-fields of neighboring metallic nanoparticles.

Fig. 3-2-1 shows the absolute value of the real part of the dielectric function of various metals, as a function of the wavelength, as determined

by using the parameter from article [96]. At the plasmon resonance condition of polarizability, the dielectric constant of the metal is twice the dielectric constant of the medium  $\epsilon_{\text{medium}}$ . In Fig. 3-2-1, the dotted line corresponds to the value of  $2\epsilon_{\text{medium}}$  and the dots denote the point of intersection with the dielectric constant of the metal. The plasmon resonance frequency varies significantly with the type of metal. The plasmon resonance frequency of Au, Ag, and Cu lies within the range of wavelengths associated with visible light.

Fig. 3-2-2 shows the imaginary part of the dielectric function (which is correlated with the energy loss within the medium) of various metals, as a function of the wavelength. The dielectric function of Au, Ag, and Cu is smaller than those of other metals in the spectrum; in fact, at wavelengths higher than 600 nm, this function is one order of magnitude smaller than those of other materials. As shown in Fig. 3-2-3, however, the quality factor of Au, Ag, and Cu is higher than those of the other metals and hence, these three metals were selected for plasma-induced dewetting.

The particle size and uniformity, as well as the interparticle distance, play a significant role in the fabrication of nanoparticle arrays. In other words, the distribution of these arrays can be modified by varying these parameters and therefore, in this study, various factors that contribute to this distribution was investigated. These include the thickness

and density of the metallic film, interfacial surface energy between the substrate and the film, roughness of the substrate, etc.

Prior to the plasma treatment, the nanoparticles increased in size with increasing film thickness. Fig. 3-2-4 and Fig. 3-2-5 show FE-SEM images of Au films after plasma-induced dewetting; these films had different initial thicknesses. A uniform nanoparticle array was obtained within 10 min of the treatment at 700 W. The morphology of the Au nanoparticle array is similar to that obtained in the case of general spinodal dewetting. However, most of the results obtained in this study on plasma-induced dewetting differ significantly from those associated with spinodal dewetting. Fig. 2-3 shows that the engineering temperature of the chamber saturates at only 544 K. This temperature is significantly lower than the melting temperatures (1337.33 K, 1234.93 K, and 1357.77 K, respectively) of Au, Ag, and Cu. Therefore, the experiments were all governed by the solid-state dewetting mechanism.

Fig. 3-2-6 shows FE-SEM images of the Ag and Cu films after the H<sub>2</sub> plasma treatment. This treatment resulted in relatively uniform metal-nanoparticle arrays, indicating that Ag and Cu undergo a similar solid-state dewetting to that of Au.

The dependence of the average diameter of the nanoparticle arrays on the thickness of the Au film is shown in Fig. 3-2-7. The diameter

increases linearly with increasing film thickness, in contrast to the  $r \sim h^{1.54}$  dependence that is typical of spinodal dewetting. Similar results were obtained in our previous work [97]. Plasma-induced dewetting progresses by means of a heterogeneous hole-nucleation mechanism, which is expected to give rise to more holes than those resulting from spinodal dewetting. The results obtained in this work show that the inter-hole spacing, growth time of the holes, and therefore the size of the nanoparticle array, decreased with increasing number of holes.

Fig. 3-2-8 shows the XRR- and RBS-determined density of the Au film as a function of the ICP power. The ICP-deposited film is denser than the film obtained via normal DC deposition. As such, the effect of the film density on the dewetting mechanism was investigated by preparing samples with the same thickness, but differing film densities. Different distributions of nanoparticle array are obtained in films with differing densities, even if the film thickness is the same.

Fig. 3-2-9 and Fig. 3-2-10 (a) show that, for the same initial thickness, the dense (i.e., ICP-deposited) Au sample had, on average, larger (125.7 nm vs. 98.1 nm) nanoparticles than its non-ICP-deposited counterpart. In addition, as Fig. 3-2-10 (b) shows, the size distribution of the dense 12.4-nm-thick sample is quite similar to that of the nanoparticle array formed by dewetting a 15.5-nm-thick non-ICP-deposited sample. These

samples have a similar total number of Au atoms, which may account for the similarity in the average nanoparticle size. Furthermore, hole nucleation is more difficult in the dense sample than in the other samples, which consist of a higher number of defects, grain boundaries, and triple junctions. The size distribution of the dense sample is therefore broader than those of the other samples (12.4-nm and 15.5-nm non-ICP-deposited films). In other words, the size distribution of the nanoparticles in the dense sample varies significantly, as evidenced by the high standard deviation.

Fig. 3-2-11 shows the FE-SEM images of samples that were subjected to a plasma treatment for 15 min at 700 W; these samples underwent plasma pre-treatments for various times. Plasma pre-treatment of the substrate (i.e., prior to deposition) enhances the interfacial energy between the substrate and the film. In fact, solid-state dewetting is induced by an imbalance between the interfacial and surface energies, and hence a high interfacial energy results in a rapid dewetting process. Therefore, the time required for the completion of dewetting and realizing nanoparticle arrays, increased with increasing pre-treatment time. These results indicate that the process time required for complete dewetting can be reduced if the interfacial energy between the substrate and the film is minimized.

In this work, an alternative method is suggested for changing the distribution of the nanoparticle array. This distribution may be changed via

repeated deposition and plasma treatment. In order to control the spatial distribution of the array, particularly the number of nanoparticles per unit area and inter-particle spacing the following experimental sequence was performed: 1st deposition, 1st plasma treatment, 2nd deposition, and 2nd plasma treatment.

Fig. 3-2-12 shows images of the films subjected to repeated dewetting; these films had different initial thicknesses. Both large and small nanoparticles were obtained when the film formed during the first deposition was thicker than that formed during the second deposition. However, appropriate processing times during these depositions resulted in arrays with a significantly higher number per unit area of nanoparticles than those fabricated via one-time dewetting. The nanoparticle sizes in samples subjected to one-time and two-time dewetting are compared in Table. 3-2-1. As the table shows, the samples have similar mean nanoparticle sizes of 15.6 and 15.8 nm respectively. The total number of particles in the latter is, however, 50% higher and the corresponding open area ratio is lower than that of the former. This indicates that, compared to the array resulting from one-time dewetting, a denser array was fabricated via two-time dewetting. After the first dewetting step of the sequence was completed, the second plasma treatment had only a weak influence on the pre-existing nanoparticles. This step exerted, however, a strong influence on the films

formed during the second deposition, owing possibly to the slight oxidation of the surface atoms of the nanoparticles during dewetting. The film formed during the second deposition then blocked the energy transfer from the first dewetting and the dewetting process was performed on the second deposition film.

Repeated dewetting of the bi-continuous film yielded unique nanostructures, as shown in Fig. 3-2-13. This bi-continuous film was fabricated by manipulating the plasma treatment time. Au was deposited on the bi-continuous structure, which was then subjected to a plasma treatment. If the inter-spacing of this film was filled with nanoparticles then, as in the case of the previous experiment, the pre-existing bi-continuous structure was only slightly affected by the second plasma treatment. This nanostructure could then be used for the dispersion and propagation of surface plasmon polaritons [10,98,99].

|                    | One-time dewetting               | Two-time dewetting   |
|--------------------|----------------------------------|--|
| Process            | 3.1 nm Dep /<br>Plasma treatment | 3.1 nm Dep / Plasma treatment /<br>4.5 nm Dep / Plasma treatment |
| Nanoparticle Size  | 15.6 nm                          | 15.8 nm  |
| Standard Deviation | 6.4 nm                           | 9.6 nm   |
| Open Area Ratio    | 79.5%                            | 64.2%  |
| Total NP Number    | 8055                             | 11762  |

Table. 3-2-1 Characteristics of the nanoparticle arrays obtained via one-time and two-time dewetting.

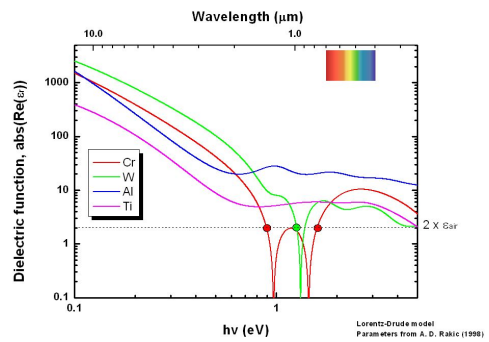
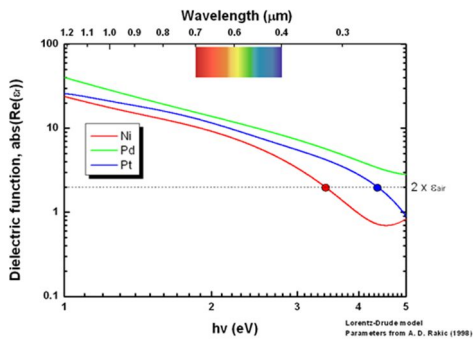
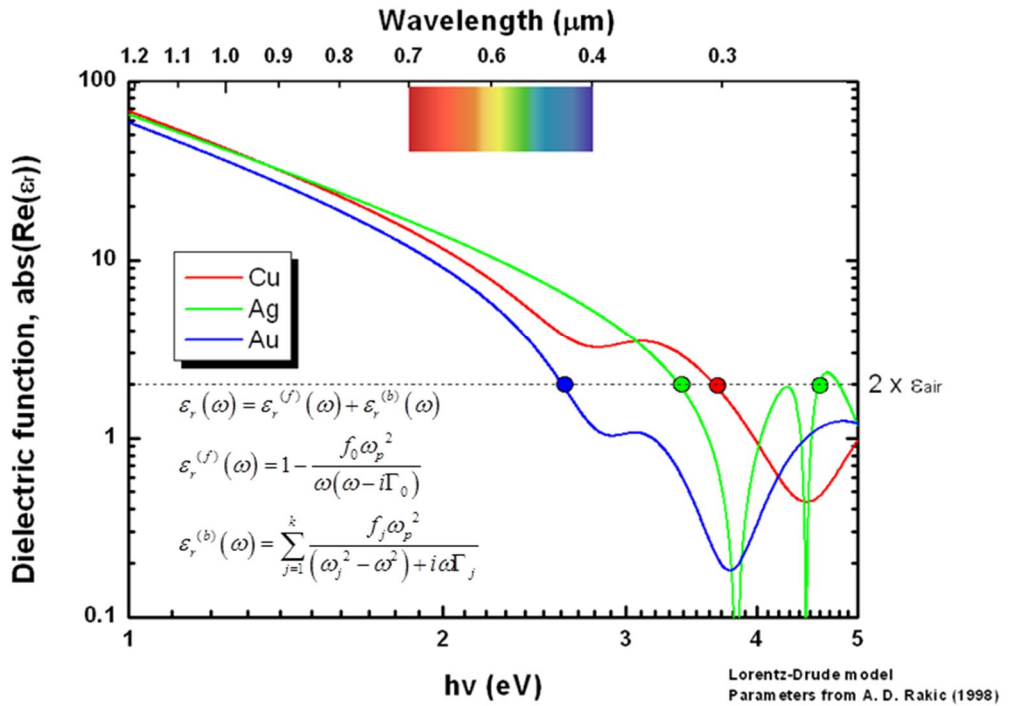


Fig. 3-2-1 Absolute value of the real part of the dielectric function, of various metals, as a function of the wavelength.

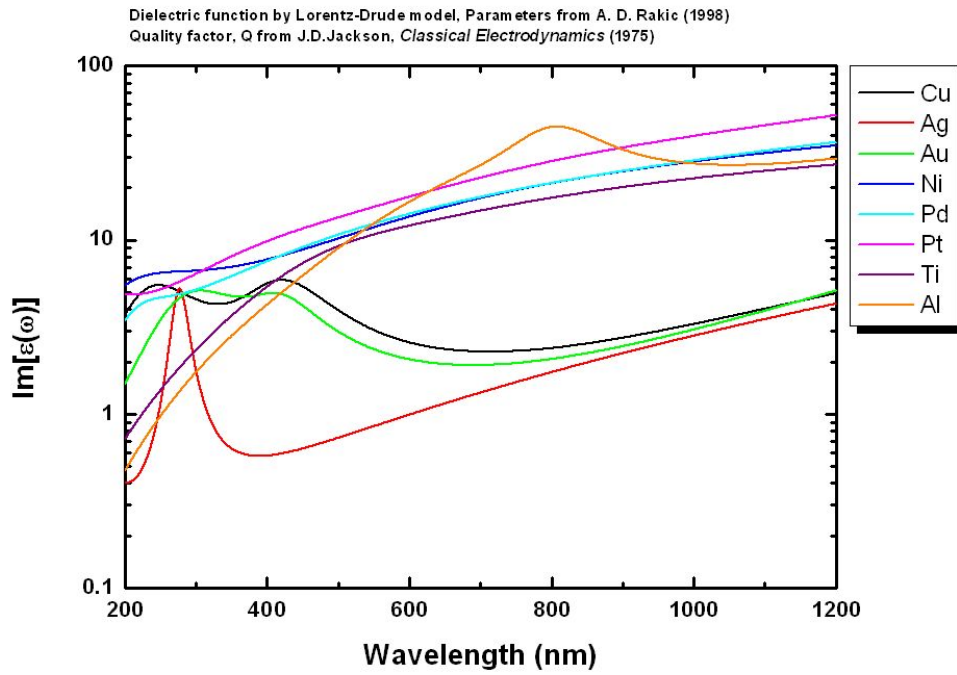


Fig. 3-2-2 Imaginary part of the dielectric function, of various metals, as a function of the wavelength.



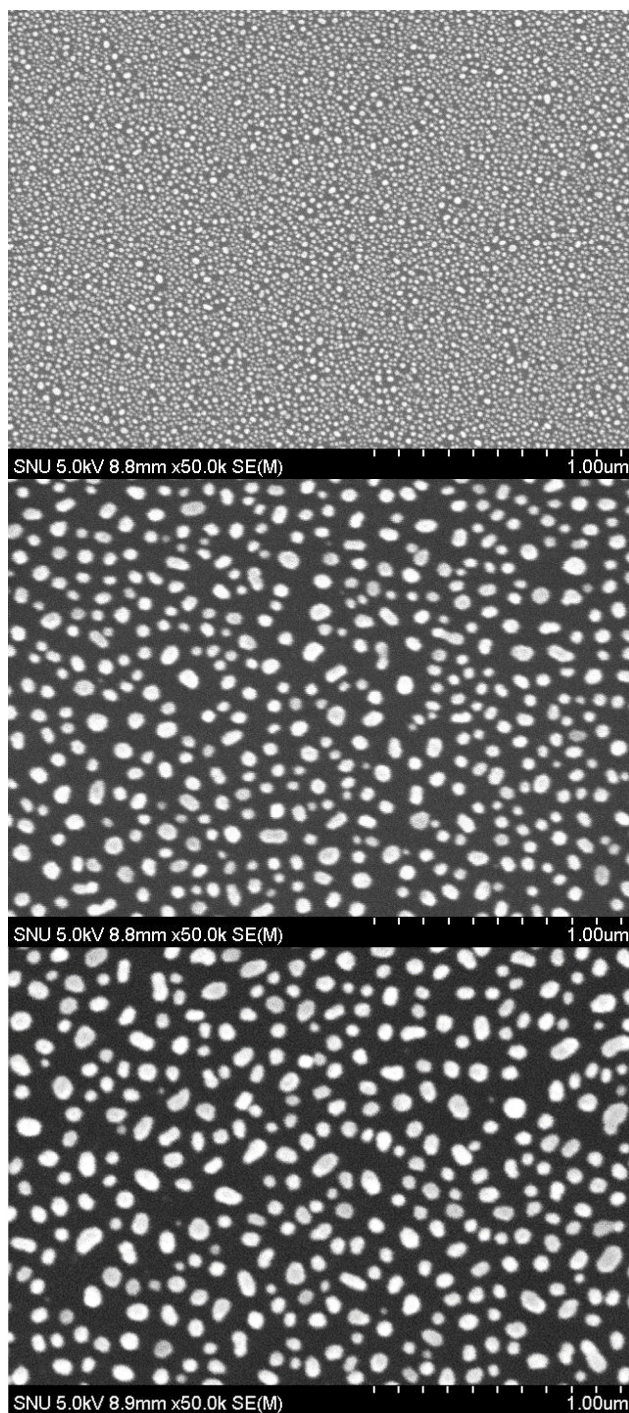


Fig. 3-2-4 Top-view FE-SEM images of 3.1-nm, 4.5-nm, and 6.2-nm-thick Au films subjected to a H<sub>2</sub> plasma treatment; the images were obtained at magnification of 50,000 $\times$ .

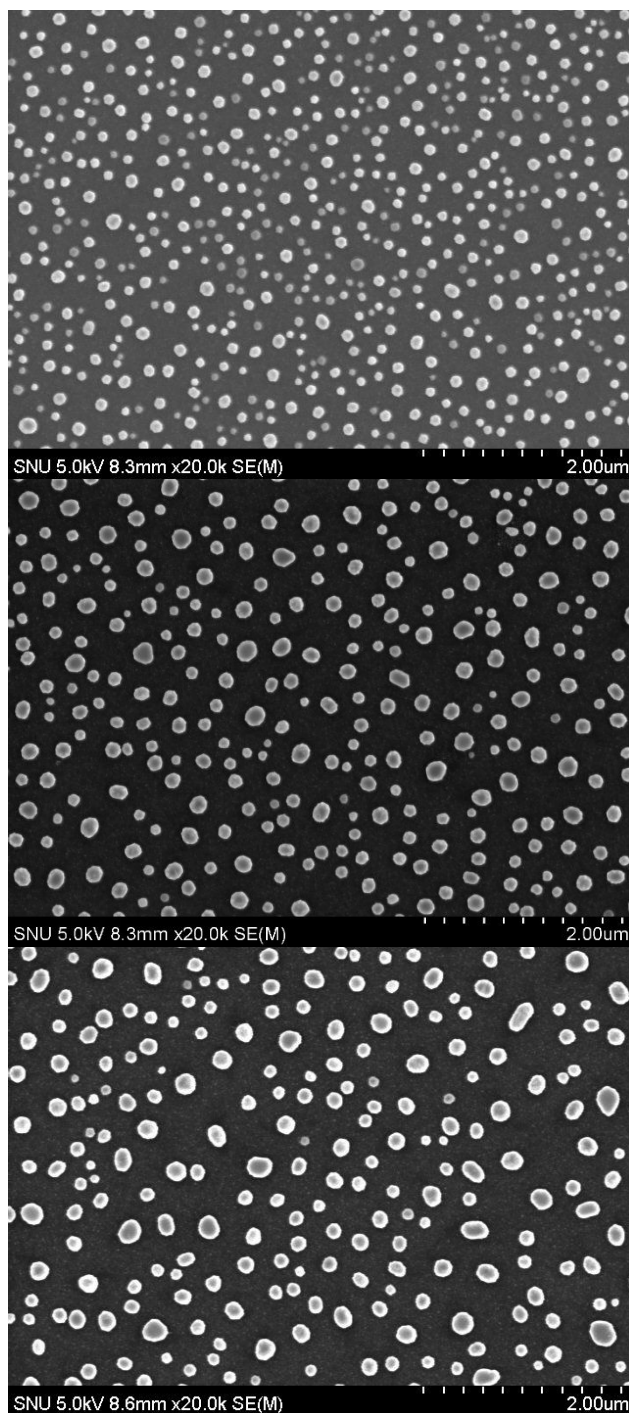


Fig. 3-2-5 Top-view FE-SEM images of 9.3-nm, 12.4-nm, and 15.5-nm-thick Au films subjected to a H<sub>2</sub> plasma treatment; the images were obtained at magnification of 20,000 $\times$ .

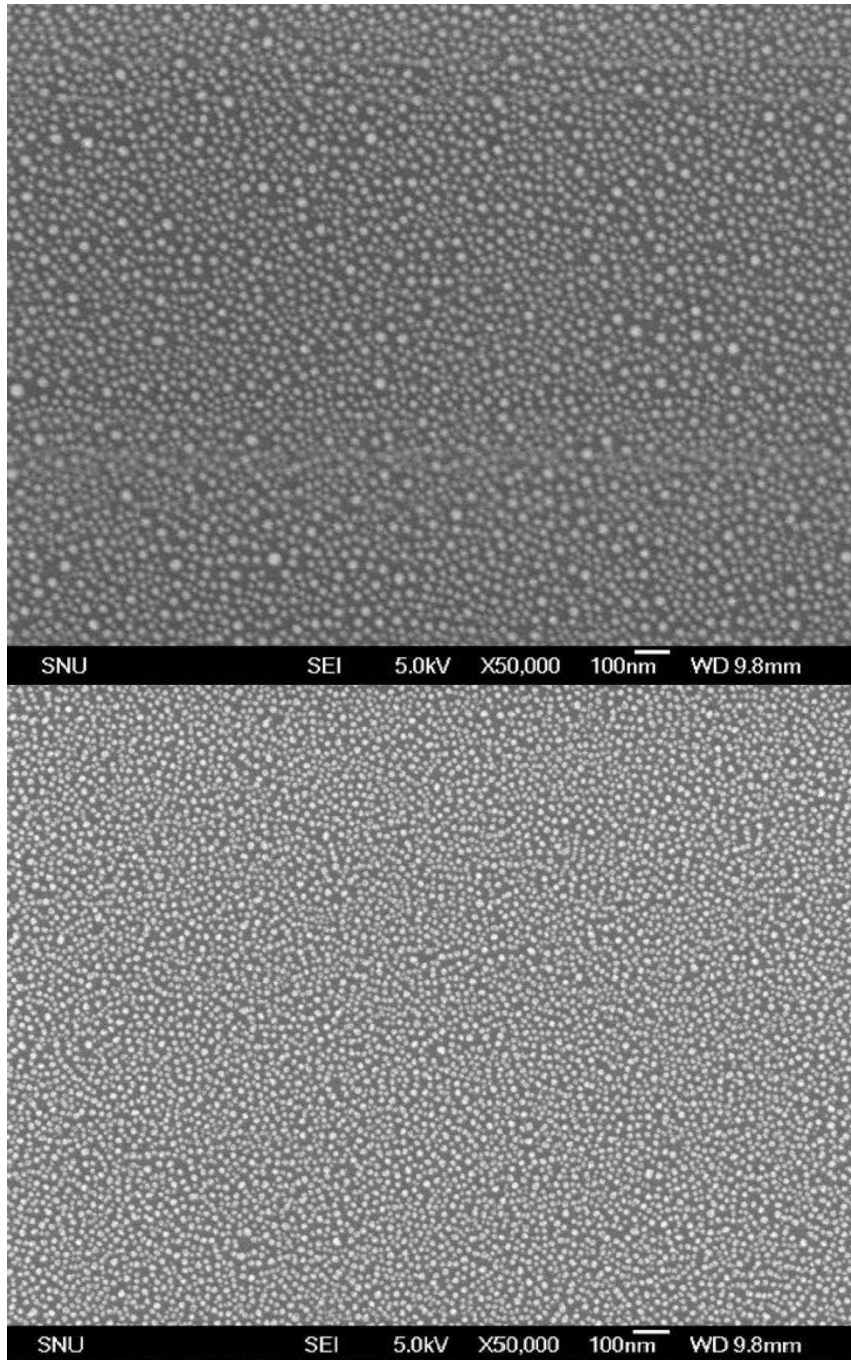


Fig. 3-2-6 FE-SEM images of Ag and Cu films subjected to a H<sub>2</sub> plasma treatment; images were obtained at a magnification of 50,000 $\times$ .

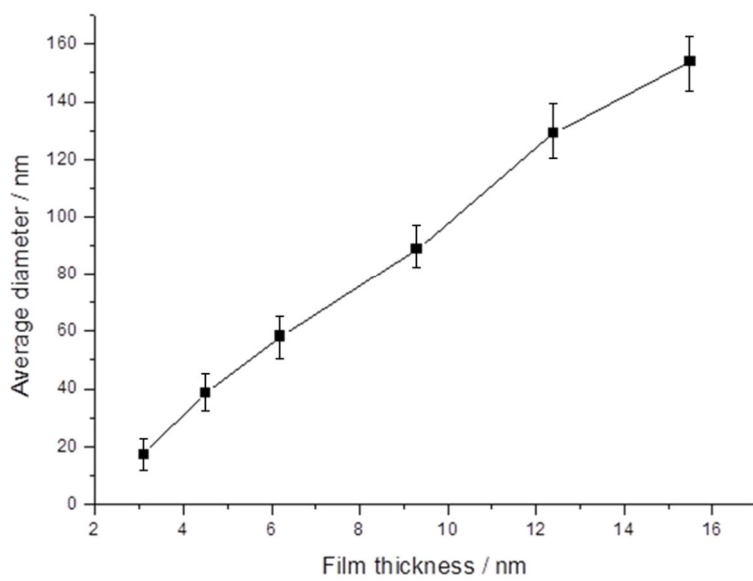


Fig. 3-2-7 Dependence of the average diameter of the nanoparticle array on the average thickness of the Au film.

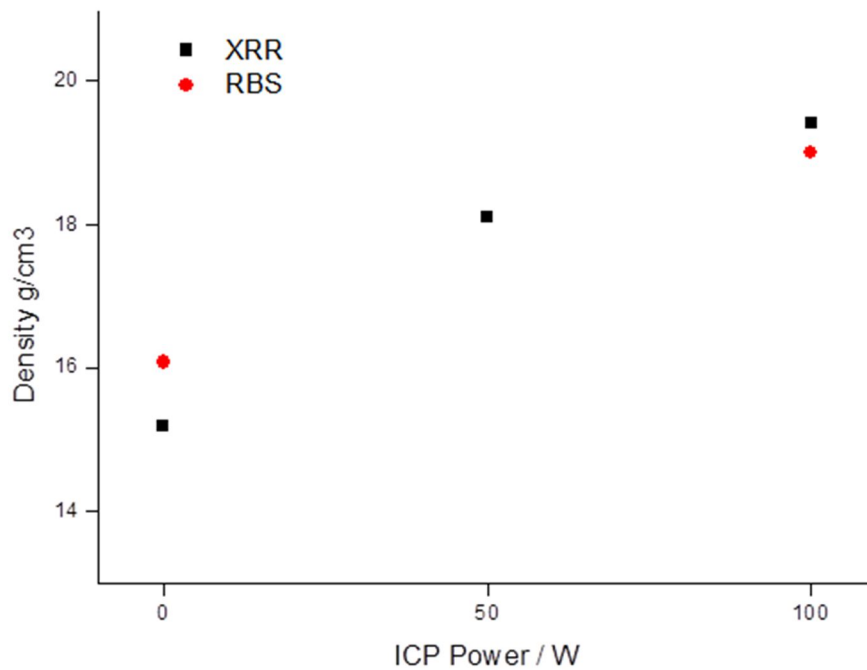


Fig. 3-2-8 Density of the Au film (as determined via X-ray reflectometry and Rutherford backscattering spectrometry) as a function of the ICP power.

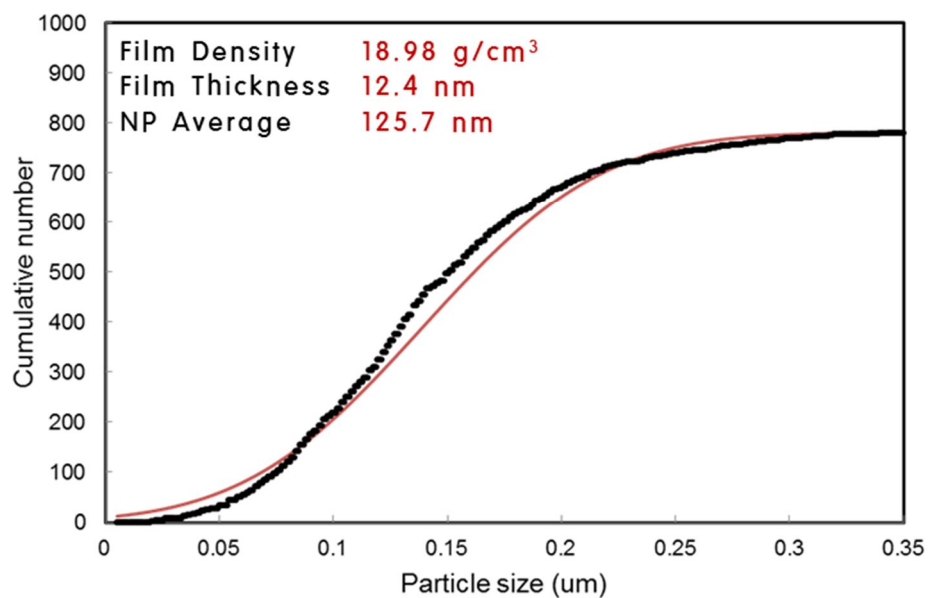
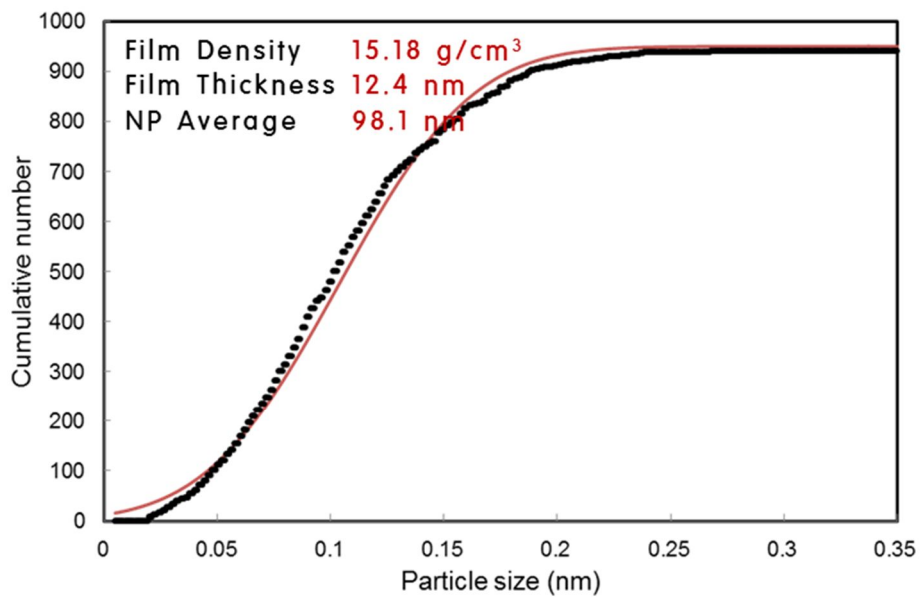


Fig. 3-2-9 Cumulative number of particle sizes of plasma-treated Au films that had differing initial densities.

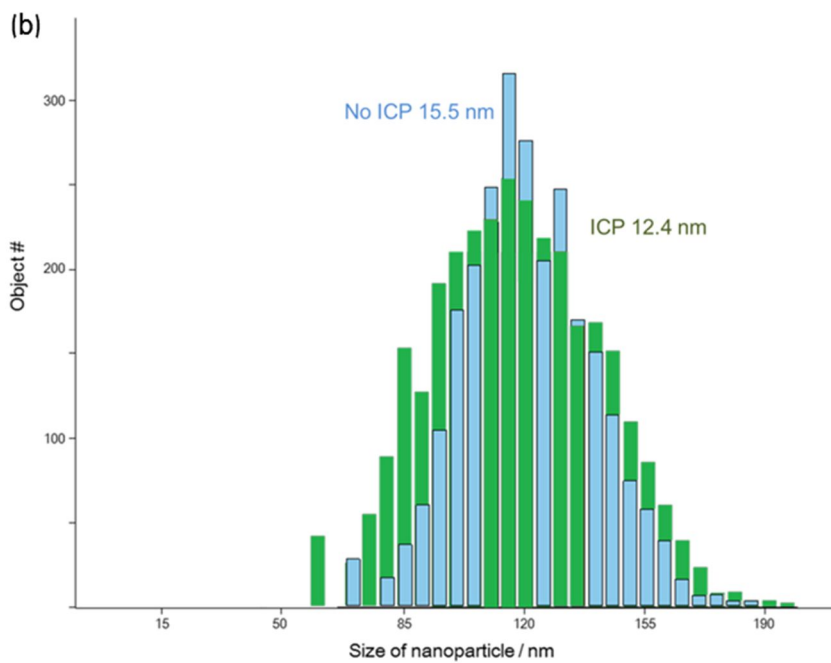
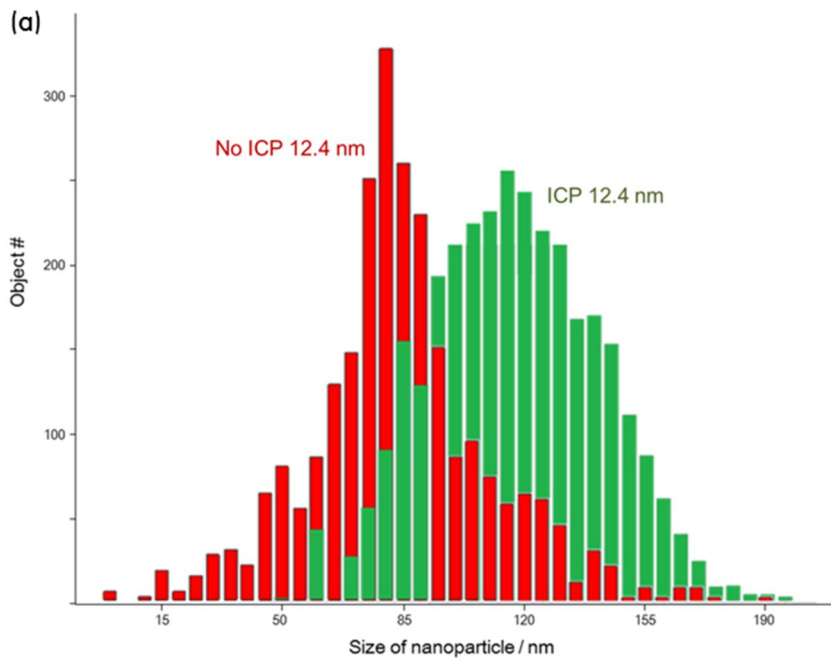


Fig. 3-2-10 Size distribution of nanoparticles formed during the dewetting of films with differing thickness and density.

## Plasma Pre-treatment of Substrate

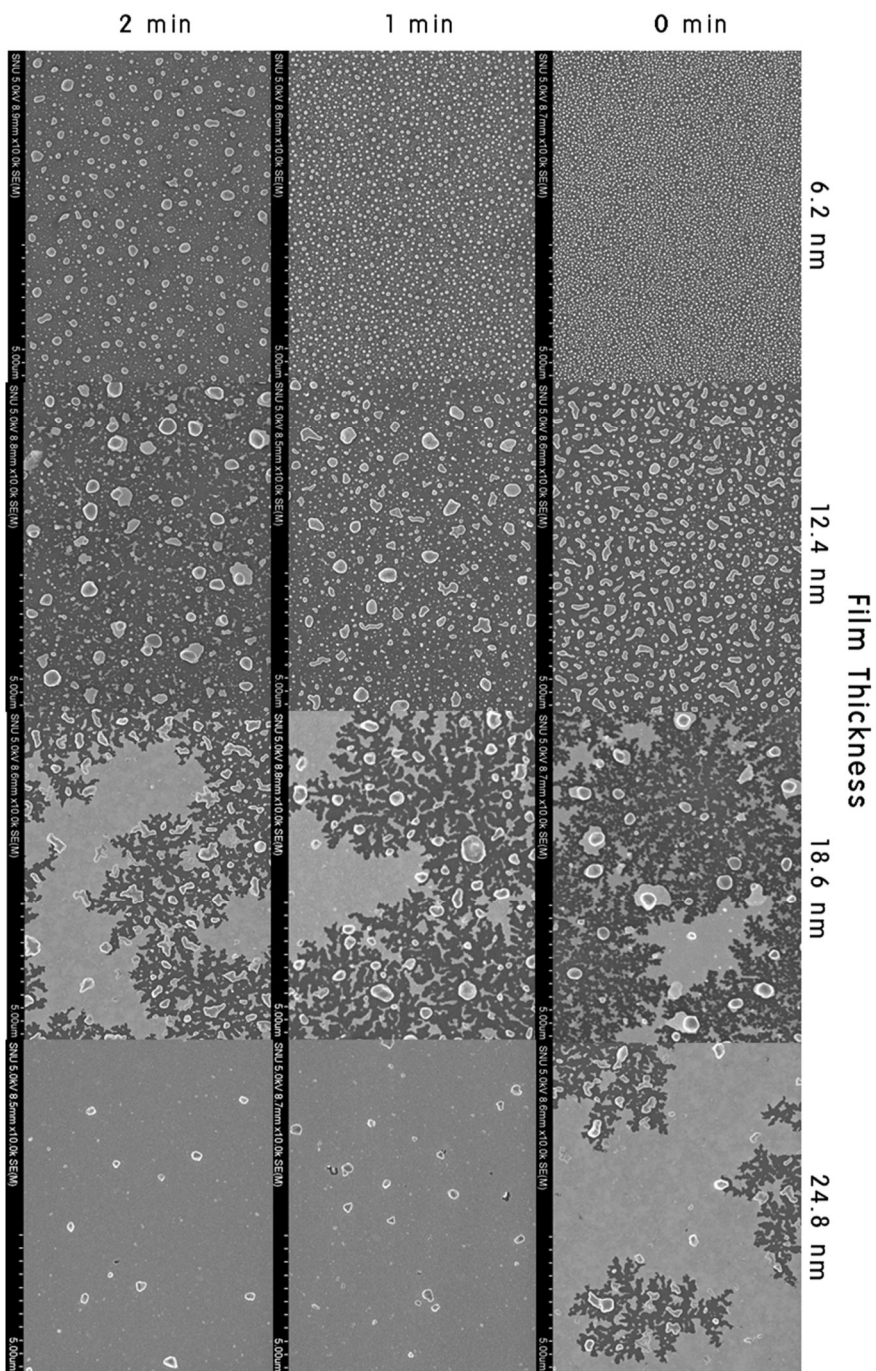


Fig. 3-2-11 FE-SEM images showing films with different initial thicknesses; these films were subjected to a plasma pre-treatment for various times, prior to a plasma treatment at 700 W for 15 min.

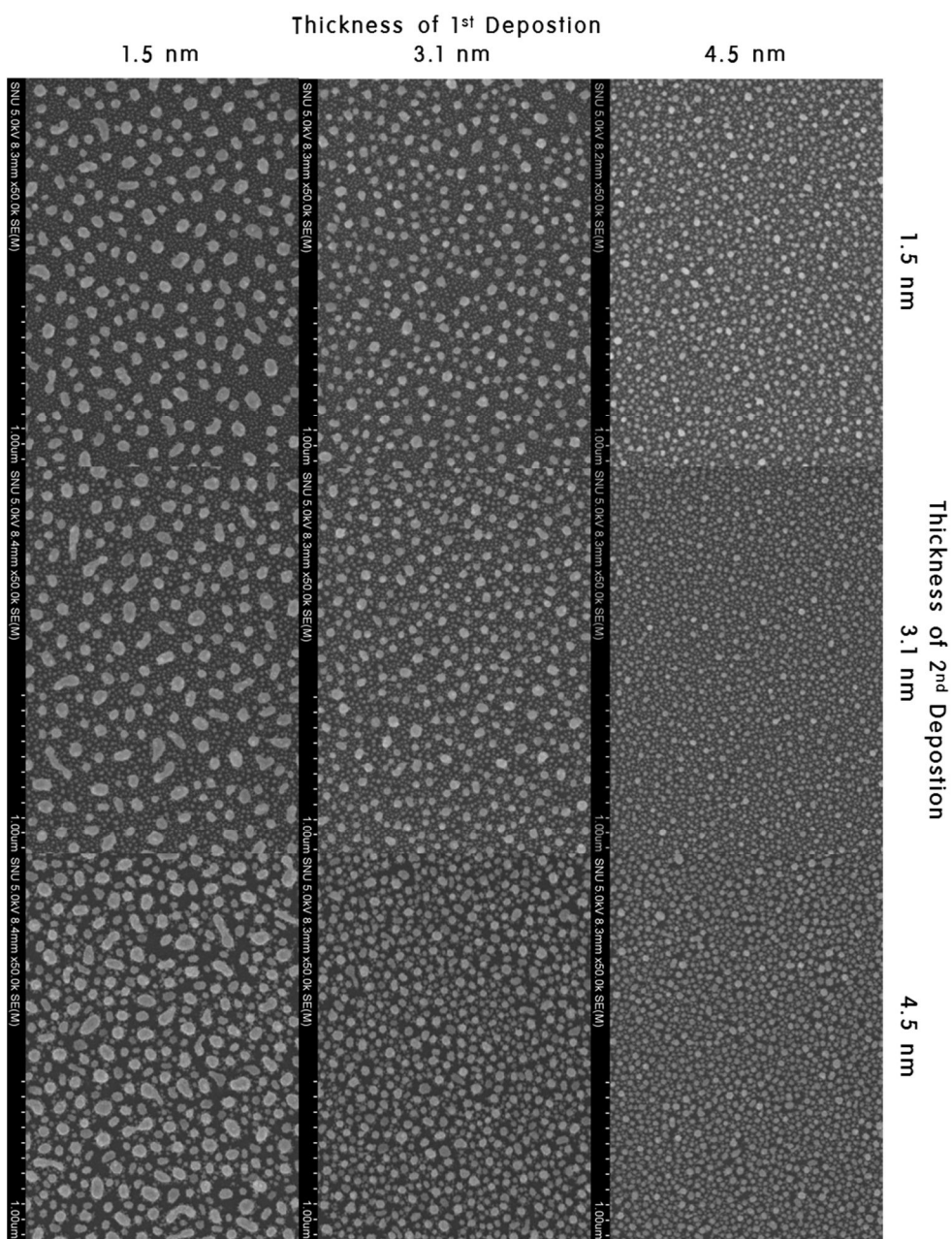


Fig. 3-2-12 FE-SEM images showing various nanoparticle arrays obtained through a repeated dewetting process that consists of two deposition steps and a plasma treatment.

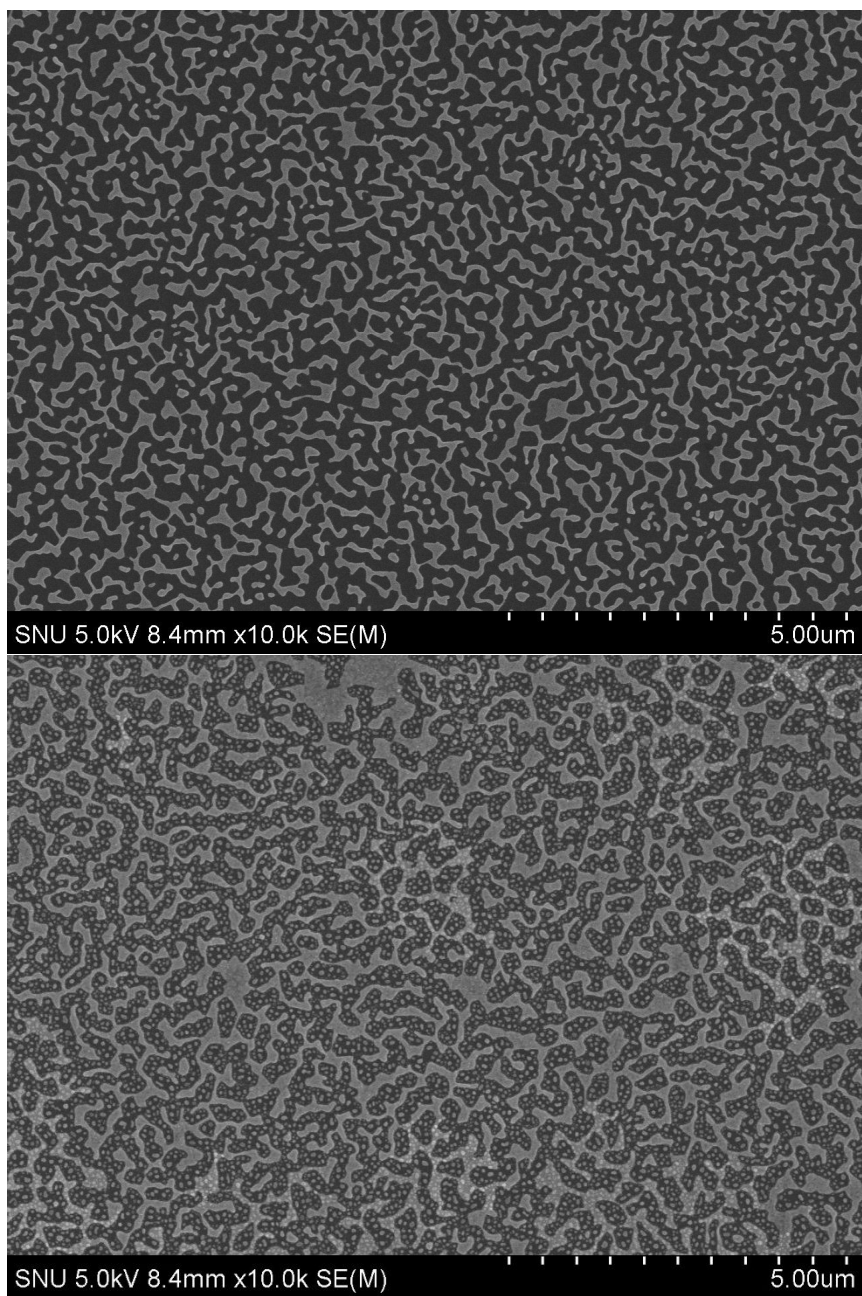


Fig. 3-2-13 FE-SEM images of nanoparticle arrays obtained via deposition on, and plasma dewetting of, a pre-existing bi-continuous structure.

## 3.3 Applications of nanostructure

### 3.3.1 Organic solar cell

Fig. 3-3-1 shows a schematic of an organic solar cell structure. In order to improve the performance of the cell, the Au-metal nanoparticle array was fabricated, via plasma-induced dewetting, on the ITO surfaces. The devices were fabricated by sandwiching a spin-coated blend of P3HT/PCBM (in a 1:1 wt.%/wt.% ratio) between a transparent anode and cathode. The anode and cathode consisted of glass substrates pre-coated with ITO, modified by a spin-coated polyethylenedioxythiophene/polystyrenesulphonate (PEDOT/PSS) layer (~40 nm), and Ca (~20 nm) capped with Al (~100 nm), respectively. The thin layer of PEDOT/PSS (Baytron P VP A1 4083), was spin-coated at 4000 rpm for 60 s. After baking at 150 °C for 10 min, the substrates were transferred to a nitrogen-filled glove box (<0.1 ppm O<sub>2</sub> and H<sub>2</sub>O). P3HT (RiekeMetals) and PCBM (Nano-C) were then dissolved in 1,2-dichlorobenzene (DCB), yielding a 40 mg mL<sup>-1</sup> solution. The blend was stirred for ~14 h at 40 °C in the glove box. The active layer was obtained by spin-coating the blend at 800 rpm for 20 s, and an active device area of 0.1 cm<sup>2</sup> was realized. Subsequently, Ca was thermally evaporated onto the active layer, and Al was then thermally

deposited onto the Ca layer under a high vacuum of  $<10^{-6}$  Torr. The plasma-induced dewetting method was used to fabricate a nanoparticle array on ITO. An appropriate plasma treatment time should be used after the Au is deposited, because excessive treatment results in damage to the substrate. Based on the aforementioned results (Chapter 3-1 / Fig. 3-1-5), the plasma treatment time was minimized in order to prevent the damage to the substrate.

The photovoltaic characteristics of each device are shown in Table 3-3-1; these include the short circuit current density ( $J_{sc}$ ), open circuit voltage ( $V_{oc}$ ), fill factor (FF), and power conversion efficiency (PCE) of the organic solar cells. Fig. 3-3-2 shows the current density-voltage (J-V) curves obtained when the nanoparticle size and number per unit area of the solar cell are varied. The size of the nanoparticles was controlled by varying the thickness of the Au film prior to dewetting. Moreover, a high density of nanoparticles was obtained through a repeated plasma-induced dewetting process (Chapter 3.2 / Fig. 3-2-12).

The samples in the nanoparticle size series all exhibited higher efficiency than the reference cell. In fact, the sample with the smallest nanoparticles (i.e., with a size of  $\sim 18$  nm) resulted in the largest increase ( $\sim 0.47\%$ ) in the PCE. The surface plasmon resonance, with near-field enhancement, was therefore attributed to the nanoparticle array. The PCE

decreased with increasing size of the nanoparticles. Arrays with nanoparticles larger than 60 nm resulted in low  $J_{sc}$ ,  $V_{oc}$  and PCE, and hence shorted devices. These low values resulted from the direct contact between the Au nanoparticles and the active layer, although a PEDOT/PSS layer was deposited above the nanoparticle array. To maximize the localized surface plasmon effect, the active layer and the nanoparticle array should be close but separate, in order to prevent recombination of the dissociated electron-hole pairs. The sample series of increasing nanoparticle number exhibited inferior results compared to the same average nanoparticle size sample series. This was expected since the effect resulting from the blocking of incident light by the array dominates that induced by near-field enhancement.

Plasma-induced dewetting was therefore successfully applied to organic solar cells. This method is versatile and hence can be applied to other organic as well as inorganic cells.

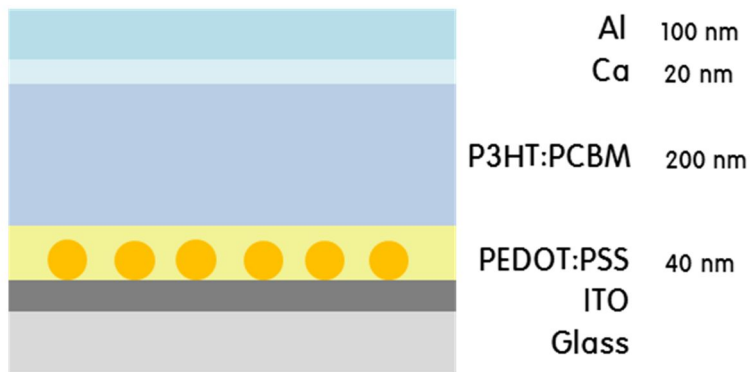


Fig. 3-3-1 Schematic of organic solar cell structure showing the Au nanoparticles deposited on the ITO, in order to enhance the efficiency via the near-field effect.

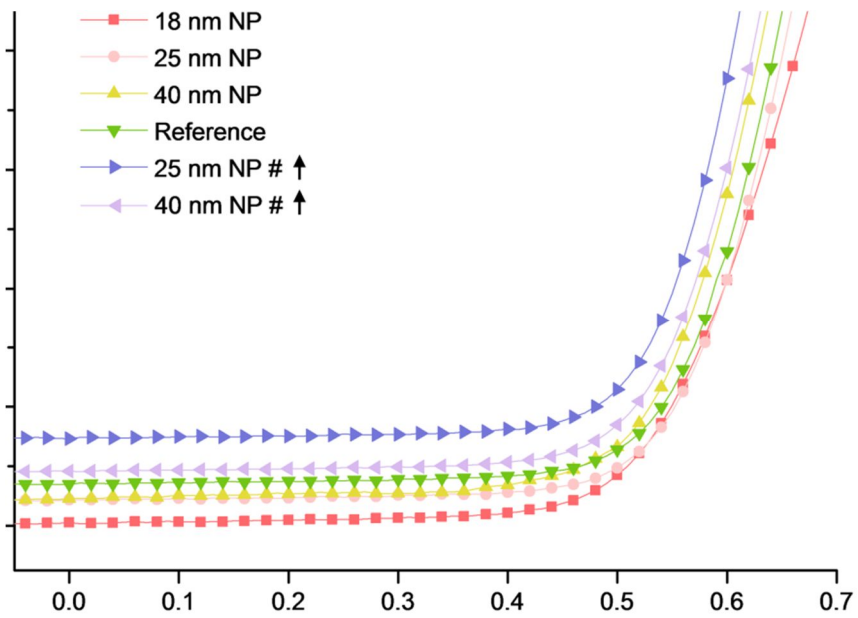


Fig. 3-3-2 Current density-voltage (J-V) curves obtained when the size and number of nanoparticles in the organic solar cell are varied.

| Nanoparticle Size | PCE<br>/ % | V <sub>oc</sub><br>/ V | J <sub>sc</sub><br>/ mAcm <sup>-2</sup> | FF<br>/ % |
|-------------------|------------|------------------------|---|-----------|
| Reference         | 2.75       | 0.58                   | 6.61                                    | 7.16      |
| 18 nm NP          | 3.22       | 0.60                   | 7.92                                    | 7.02      |
| 18 nm NP High #   | 2.79       | 0.59                   | 6.58                                    | 7.21      |
| 25 nm NP          | 3.01       | 0.59                   | 7.13                                    | 7.11      |
| 25 nm NP High #   | 2.62       | 0.56                   | 6.16                                    | 7.21      |
| 40 nm NP          | 2.87       | 0.58                   | 7.12                                    | 6.87      |
| 40 nm NP High #   | 2.01       | 0.55                   | 5.07                                    | 7.18      |

Table. 3-3-1 Photovoltaic characteristics obtained when the size and number of nanoparticles in the organic solar cell are varied.

### 3.3.2 Photocatalytic Activity

An ~600-nm-thick layer of anatase TiO<sub>2</sub>, as shown in Fig. 3-3-3 (a), was deposited via ICP-assisted magnetron sputtering. Fig. 3-3-3 (b) and (c) show Au films that were deposited on the TiO<sub>2</sub> and subjected to a plasma treatment in order to fabricate nanoparticle arrays. The photocatalytic activity was measured by means of MB photo-degradation after 2 h of illumination by UV and visible(Vis) light. UV spectra were collected over wavelengths ranging from 200–800 nm, from the MB (10<sup>-4</sup> M) solution after irradiation using TiO<sub>2</sub> and TiO<sub>2</sub> / Au nanoparticle arrays. Fig. 3-3-4 shows the absorption spectra collected from MB before and after 2 h of irradiation. As the figure shows, the absorbance of the solution associated with the samples is, in all cases, lower than that of the MB solution only; the samples used were bare TiO<sub>2</sub> sample, Au-NP array/TiO<sub>2</sub> samples with 25-nm nanoparticles (NPs), 40-nm NPs, and increasing number of NP (obtained via repeated dewetting) sample. Among all samples, the sample that underwent repeated dewetting exhibited the highest rate of MB photo-degradation. The absorbance of the MB decreased only slightly in the case of the bare TiO<sub>2</sub> sample irradiated with visible light. However, the Au nanoparticle array on TiO<sub>2</sub> samples exhibited a relatively large reduction in absorbance, albeit lower than that occurring during UV irradiation.

The possible mechanisms governing the effect of Au-NP array/TiO<sub>2</sub> on the degradation of azo dyes under UV and Vis light have been described as follows “Under UV light irradiation, TiO<sub>2</sub> could be photoexcited and produced h<sup>+</sup> and e<sup>-</sup> pair. The recombination rate of h<sup>+</sup> and e<sup>-</sup> pair is restrained as the electrons migrate to Au. So, the superoxide and hydroxyl radical production rate improves as shown in Fig. 3-3-5. On the other hand, under visible light irradiation, the possible reaction mechanism of degradation on Au-TiO<sub>2</sub> is that Au was photoexcited due to the surface plasmon resonance effect and then photogenerated electrons were injected into O<sub>2</sub> adsorbed on TiO<sub>2</sub> as shown in Fig. 3-3-6. Therefore, the production of superoxide and hydroxyl radicals in presence of O<sub>2</sub> was accelerated [100].”

The Au-nanoparticle array fabricated via plasma-induced dewetting played a supporting role to TiO<sub>2</sub> in enhancing the photocatalytic activity. In fact, the repeated dewetting employed in this work yielded a high number of nanoparticles and the best results of all the experiments performed.

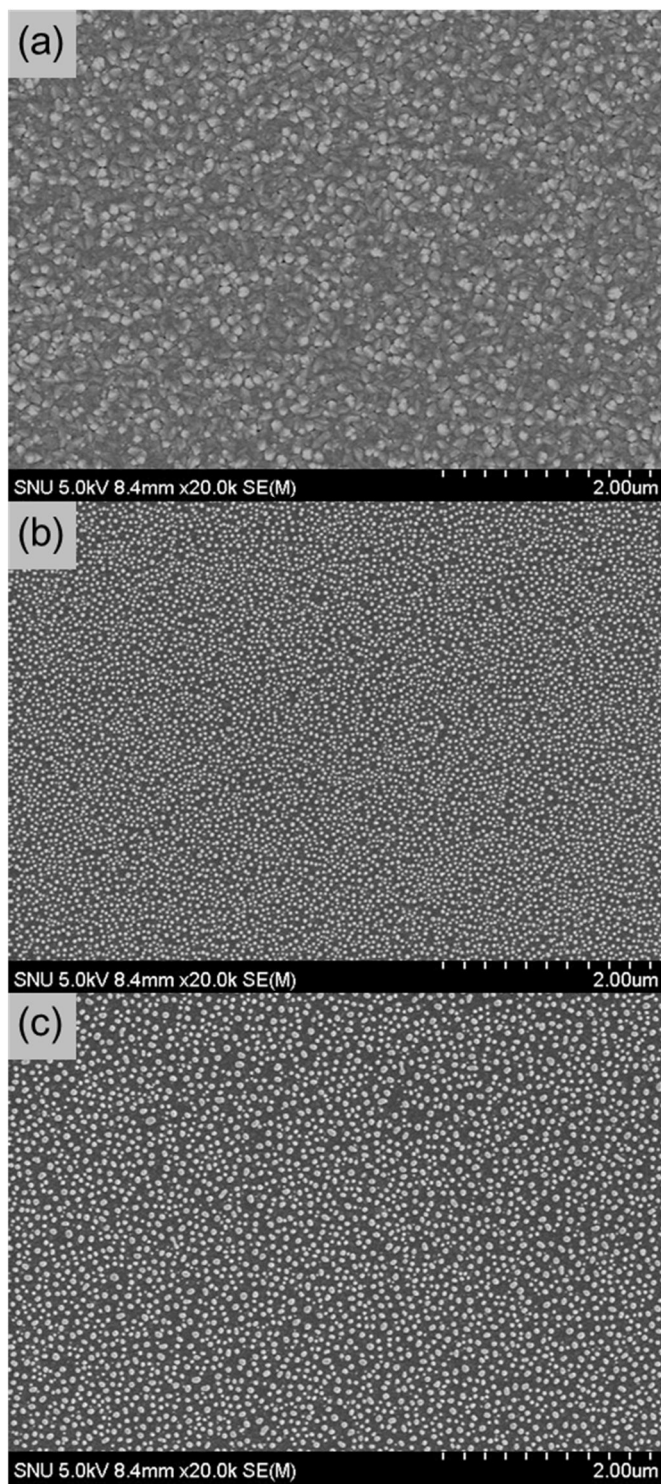


Fig. 3-3-3 FE-SEM images of (a)  $\text{TiO}_2$  on quartz, (b) 27-nm Au-nanoparticle array on  $\text{TiO}_2$  and (c) 43-nm Au-nanoparticle array.

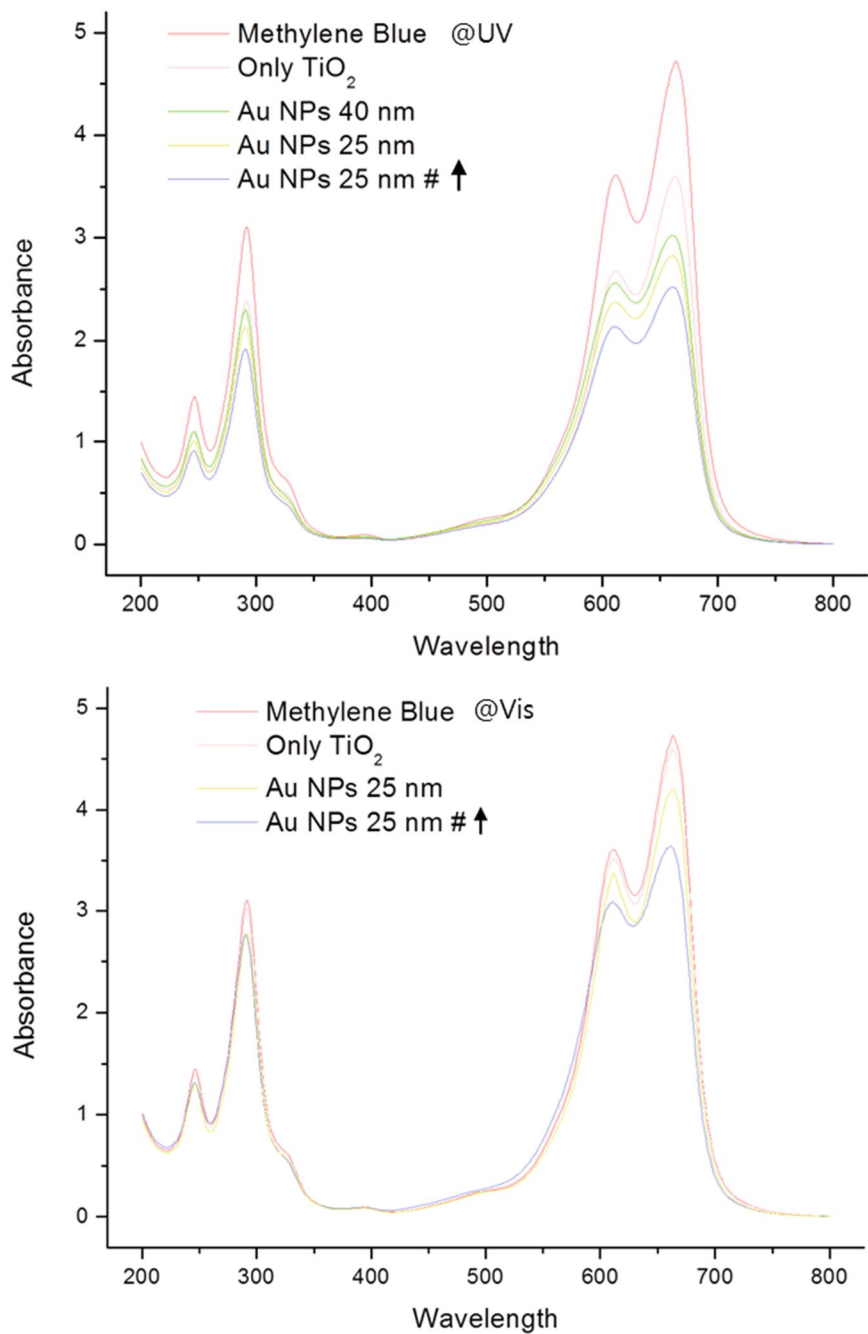


Fig. 3-3-4 UV spectra collected after 2 h UV-Vis illumination of a methylene blue solution associated with various TiO<sub>2</sub> and Au-nanoparticle samples.

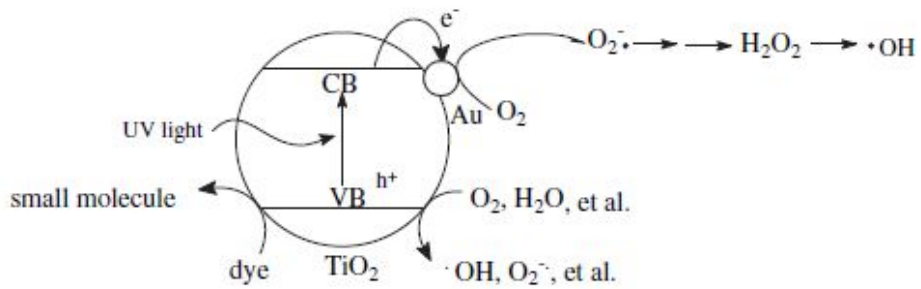


Fig. 3-3-5 A reaction mechanism of Au-TiO<sub>2</sub> for the degradation of azo dyes under UV light irradiation [100].

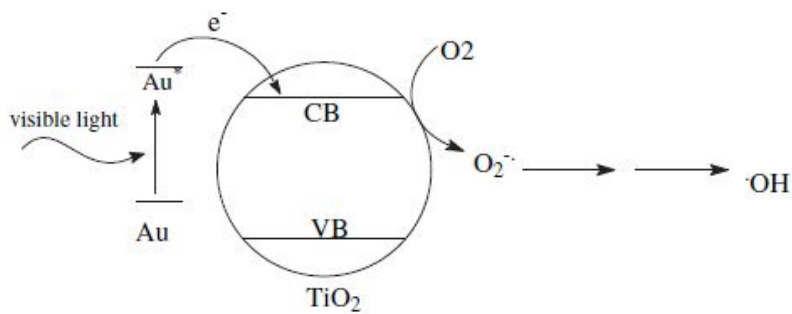


Fig. 3-3-6 A reaction mechanism of Au-TiO<sub>2</sub> for the degradation of azo dyes under visible light irradiation [100].

### 3.3.3 Transparent conductive electrodes

Bi-continuous Au nano-films were easily fabricated by using the plasma-induced dewetting method. The dewetting process progressed as follows: hole nucleation, hole growth, bi-continuous film formation, and nanoparticle array formation. Therefore, in order to fabricate a bi-continuous nano-film, the plasma treatment time should be controlled before the film becomes a nanoparticle array. Fig. 3-3-7 shows the FE-SEM images of bi-continuous Au nano-films formed by subjecting films of various initial thicknesses to a plasma treatment. The open area, i.e., the region of the substrate exposed, ranges from 25–60%. Fig. 3-3-7 (a) shows that, in the initial stage of the bi-continuous structure, the Au film covers a significant fraction (~75%) of the quartz surface. Therefore, the transmittance was inadequate for TCE. Excessive periods of plasma treatment, as shown in Fig. 3-3-7 (d) lead, however, to fragmentation of the film and consequently, a significant increase in the sheet resistance. The results indicate that the optimum bi-continuous film, from the viewpoint of sheet resistivity and transmittance, is obtained at an open area of 50–60%.

The dependence of the sheet resistance and transmittance on the thickness of the bare Au films is shown in Fig. 3-3-8. As the figure shows, the sheet resistance and the transmittance decreased with increasing film

thickness. Sufficiently thick Au films are essential to satisfying the sheet resistance requirement of TCE. The size of the open area increased continuously with the progression of dewetting and the transmittance increased. However, the plasma treatment should be carefully conducted in order to minimize the conductivity loss and hence avoid TCE failure owing to the sheet resistance.

The sheet resistance and transmittance of successfully fabricated bi-continuous structures are listed in Table. 3-3-2. Each transmittance value was calculated by averaging the respective transmittance measured at wavelengths ranging from 200–800 nm during UV spectroscopy. Compared to those obtained via DC sputtering, Au films deposited via ICP-assisted sputtering are denser (Fig. 3-2-8) and therefore, required a longer plasma treatment time for the fabrication of a bi-continuous structure. The bi-continuous ICP-deposited films were inferior to their DC-sputtered counterparts, from both a sheet resistance and transmittance viewpoint.

This results possibly from the plasma-treatment-induced damage to the quartz substrate and films. Excellent results were attained in the case of bi-continuous films fabricated via DC sputter deposition and an optimized plasma treatment. Plasma-induced dewetting for TCE results in a sheet resistance and transmittance of  $<100 \text{ } \Omega/\text{sq.}$  and 75–83%, respectively. Therefore, this method is superior to other methods used for fabricating

metal-nanostructure-based electrodes [75–83].

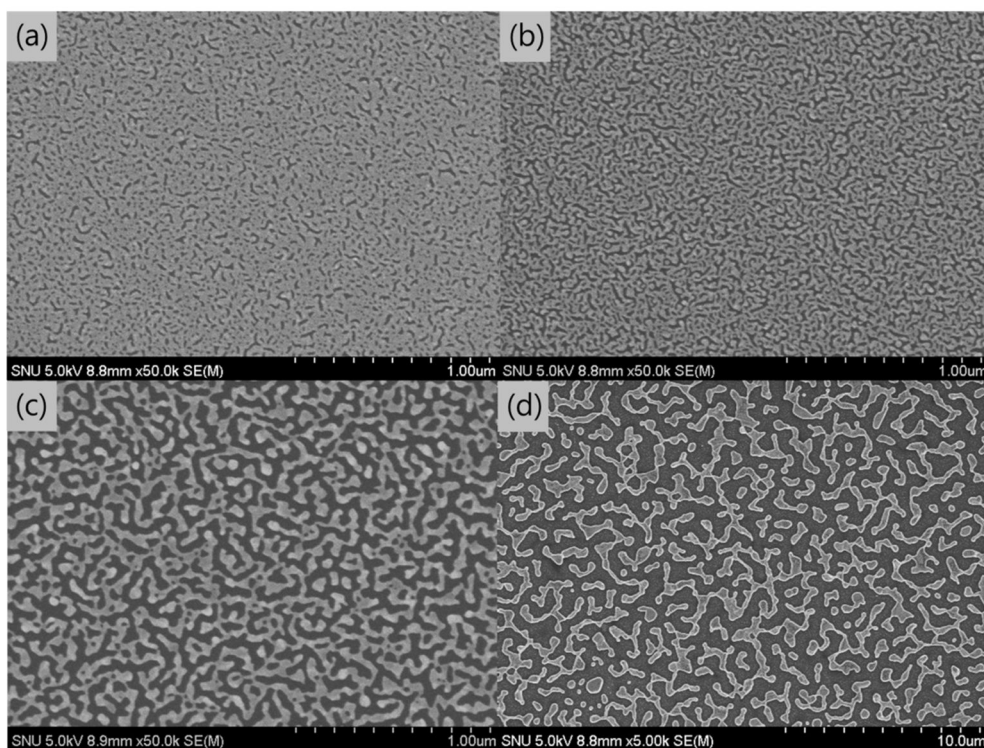


Fig. 3-3-7 FE-SEM images of bi-continuous Au nanostructures obtained via the plasma treatment of films with various initial thicknesses. The open area, i.e., region of the substrate that is exposed, ranges from 30–70%.

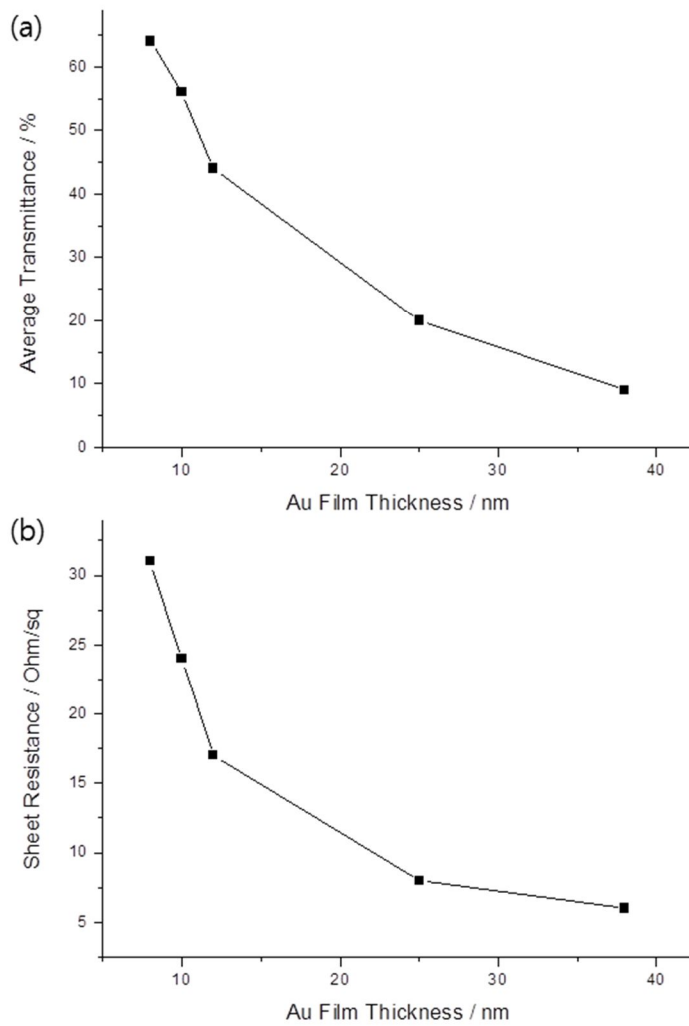


Fig. 3-3-8 Dependence of the sheet resistance and transmittance on the thickness of the Au film deposited on quartz.

| DC Sputter Deposition   | Transmittance (%) | Sheet Resistance ( $\Omega/\text{sq.}$ ) |
|-------------------------|-------------------|--|
| 6-nm Bi-continuous      | 83.3              | 153.2                                    |
| 6-nm dewetting complete | 85.8              | X  |
| 8-nm Bi-continuous      | 75.7              | 81.3                                     |
| 8-nm dewetting          | 78.9              | X  |
| ICP Sputter Deposition  | Transmittance (%) | Sheet Resistance ( $\Omega/\text{sq.}$ ) |
| 6-nm Bi-continuous      | 80.4              | 220.6                                    |
| 6-nm dewetting complete | 87.1              | X  |
| 8-nm Bi-continuous      | 74.4              | 163.5                                    |
| 8-nm dewetting          | 76.7              | X  |

Table. 3-3-2 Transmittance and sheet resistance data from different stages of the dewetting process of DC- and ICP-sputter-deposited 6- and 8-nm-thick Au films.

## IV. CONCLUSION

Metal (Au, Ag, Cu) nanoparticle arrays and bi-continuous films were fabricated by using the plasma-induced dewetting method. In contrast to other methods, this process is rapid and can be performed at low temperatures, and over large-scaled regions. The evolution of solid-state dewetting and the open area were determined as a function of the plasma treatment time.

Many holes were nucleated at the grain boundaries and triple junctions, thereby resulting in uniform nanoparticle arrays. In addition, the time required for the completion of dewetting was lower than that associated with thermal dewetting. This resulted possibly from ion bombardment, which transfers a high amount of energy to the surface atoms, thereby leading to a higher number of holes than that formed during thermal dewetting.

The distribution of the nanoparticle array was controlled by varying parameters such as the film thickness, plasma treatment time, film density, and interfacial energy between the film and the substrate. In fact, a repeated dewetting process that resulted in significant changes in the nanoparticle array distribution was introduced. By using this method, dense nanoparticle arrays with a high number of NPs per area, mixed NP sizes,

and NP-filling of open areas in the bi-continuous films were realized.

Various Au-nanoparticle arrays were distributed on ITO, for application to organic solar cells. Based on the results, an optimum condition is suggested for maximizing the PCE via the localized surface plasmon near-field enhancement effect. Au nanoparticles on the ITO resulted in an increase (from 2.75% to 3.22%) in the PCE.

The Au-nanoparticle array plays a supporting role to  $\text{TiO}_2$  in photocatalytic activity that leads to enhanced efficiency of the system. In fact, repeated plasma-induced dewetting, which yielded a high number of nanoparticles, resulted in the lowest level of MB photo-degradation.

Bi-continuous Au films fabricated at the optimum conditions of plasma treatment, were applied to TCE. These films had excellent sheet resistance and transmittance, indicating that plasma-induced dewetting is superior to the other methods used to fabricate metal-nanostructure-based electrodes.

## V. References

- [1] S. S. Kim, et al., "Plasmon enhanced performance of organic solar cells using electrodeposited Ag nanoparticles", *Appl. Phys. Lett.*, Vol.93, No.7, 2008,
- [2] J. H. Lee, et al., "High efficiency polymer solar cells with wet deposited plasmonic gold nanodots", *Organic Electronics: physics, materials, applications*, Vol.10, No.3, 2009, pp.416-420.
- [3] J. Wang, et al., "Effect of plasmonic Au nanoparticles on inverted organic solar cell performance", *Journal of Physical Chemistry C*, Vol.117, No.1, 2013, pp.85-91.
- [4] J. L. Wu, et al., "Surface plasmonic effects of metallic nanoparticles on the performance of polymer bulk heterojunction solar cells", *ACS Nano*, Vol.5, No.2, 2011, pp.959-967.
- [5] M. J. Beliatis, et al., "Organic solar cells with plasmonic layers formed by laser nanofabrication", *PCCP*, Vol.15, No.21, 2013, pp.8237-8244.
- [6] M. Kang, et al., "Repeated Solid-state Dewetting of Thin Gold Films for Nanogap-rich Plasmonic Nanoislands", *Scientific Reports*, Vol.5, 2015,
- [7] S. Kodambaka, et al., "Germanium nanowire growth below the eutectic temperature", *Science*, Vol.316, No.5825, 2007, pp.729-732.

- [8] K. Melanie, et al., "Solid Au nanoparticles as a catalyst for growing aligned ZnO nanowires: a new understanding of the vapour–liquid–solid process", *Nanotechnology*, Vol.18, No.36, 2007, pp.365304.
- [9] J. Li, et al., "Plasmonic gold nanoparticles modified titania nanotubes for antibacterial application", *Appl. Phys. Lett.*, Vol.104, No.26, 2014, pp.261110.
- [10] W. Hou, et al., "Plasmonic enhancement of photocatalytic decomposition of methyl orange under visible light", *J. Catal.*, Vol.277, No.2, 2011, pp.149-153.
- [11] A. Umer, et al., "Selection of a suitable method for the synthesis of copper nanoparticles", *Nano*, Vol.7, No.5, 2012,
- [12] B. Khodashenas, et al., "Synthesis of silver nanoparticles with different shapes", *Arabian Journal of Chemistry*, 2015,
- [13] M. H. Lee, et al., "Fabrication of ultra-high-density nanodot array patterns (~3 Tbits/in.<sup>2</sup>) using electron-beam lithography", *Journal of Vacuum Science and Technology B: Nanotechnology and Microelectronics*, Vol.29, No.6, 2011,
- [14] M. Khan, et al., "Extension of x-ray lithography to 50 nm with a harder spectrum", *Journal of Vacuum Science and Technology B: Microelectronics and Nanometer Structures*, Vol.17, No.6, 1999, pp.3426-3432.

- [15] T. Kitayama, et al., "Proposal for a 50 nm proximity X-ray lithography system and extension to 35 nm by resist material selection", *Journal of Vacuum Science and Technology B: Microelectronics and Nanometer Structures*, Vol.18, No.6, 2000, pp.2950-2954.
- [16] F. S. S. Chien, et al., "Nanomachining of (110)-oriented silicon by scanning probe lithography and anisotropic wet etching", *Appl. Phys. Lett.*, Vol.75, No.16, 1999, pp.2429-2431.
- [17] S. Y. Chou, et al., "Sub-10 nm imprint lithography and applications", *Journal of Vacuum Science and Technology B: Microelectronics and Nanometer Structures*, Vol.15, No.6, 1997, pp.2897-2904.
- [18] B. H. Lee, et al., "High-resolution patterning of aluminum thin films with a water-mediated transfer process", *Adv. Mater.*, Vol.19, No.13, 2007, pp.1714-1718.
- [19] L. Qian, et al., "Nanoscale convection assisted self-assembly of nanoparticle monolayer", *J. Mater. Chem.*, Vol.22, No.11, 2012, pp.4932-4937.
- [20] J. Li, et al., "Template- And vacuum-ultraviolet-assisted fabrication of a Ag-nanoparticle array on flexible and rigid substrates", *Adv. Mater.*, Vol.19, No.9, 2007, pp.1267-1271.

- [21] J. Y. Kwon, et al., "Comparison of the agglomeration behavior of Au and Cu films sputter deposited on silicon dioxide", *J. Appl. Phys.*, Vol.93, No.6, 2003, pp.3270-3278.
- [22] J. Trice, et al., "Novel self-organization mechanism in ultrathin liquid films: Theory and experiment", *Phys. Rev. Lett.*, Vol.101, No.1, 2008,
- [23] J. Trice, et al., "Pulsed-laser-induced dewetting in nanoscopic metal films: Theory and experiments", *Physical Review B - Condensed Matter and Materials Physics*, Vol.75, No.23, 2007,
- [24] D. Wang, et al., "Solid-state dewetting for fabrication of metallic nanoparticles and influences of nanostructured substrates and dealloying", *Physica Status Solidi (A) Applications and Materials Science*, Vol.210, No.8, 2013, pp.1544-1551.
- [25] C. V. Thompson, Solid-state dewetting of thin films, in *Annual Review of Materials Research* vol. 42, ed, 2012, pp. 399-434.
- [26] P. A. Martin, "Thermal grooving by surface diffusion: Mullins revisited and extended to multiple grooves", *Quarterly of Applied Mathematics*, Vol.67, No.1, 2009, pp.125-136.
- [27] A. M. Thron, et al., "In-situ observation of equilibrium transitions in Ni films; agglomeration and impurity effects", *Ultramicroscopy*, Vol.137, 2014, pp.55-65.

- [28] H. Krishna, et al., "Functional nanostructures through nanosecond laser dewetting of thin metal films", JOM, Vol.60, No.9, 2008, pp.37-42.
- [29] S. J. Henley, et al., "Pulsed-laser-induced nanoscale island formation in thin metal-on-oxide films", Physical Review B, Vol.72, No.19, 2005, pp.195408.
- [30] J. Lian, et al., "Patterning metallic nanostructures by ion-beam-induced dewetting and rayleigh instability", Nano Lett., Vol.6, No.5, 2006, pp.1047-1052.
- [31] Y. Kojima, et al., "Nanoparticle formation in Au thin films by electron-beam-induced dewetting", Nanotechnology, Vol.19, No.25, 2008,
- [32] D. M. Schaadt, et al., "Enhanced semiconductor optical absorption via surface plasmon excitation in metal nanoparticles", Appl. Phys. Lett., Vol.86, No.6, 2005, pp.1-3.
- [33] D. H. Wang, et al., "Enhanced power conversion efficiency in PCDTBT/PC 70 BM bulk heterojunction photovoltaic devices with embedded silver nanoparticle clusters", Advanced Energy Materials, Vol.1, No.5, 2011, pp.766-770.
- [34] K. Kim, et al., "Roles of Au and Ag nanoparticles in efficiency enhancement of poly(3-octylthiophene)/C 60 bulk heterojunction photovoltaic devices", Appl. Phys. Lett., Vol.87, No.20, 2005, pp.1-3.

- [35] X. Yang, et al., "Plasmon enhanced light absorption in bulk heterojunction organic solar cells", *Physica Status Solidi - Rapid Research Letters*, Vol.6, No.5, 2012, pp.199-201.
- [36] M. Xue, et al., "Charge-carrier dynamics in hybrid plasmonic organic solar cells with Ag nanoparticles", *Appl. Phys. Lett.*, Vol.98, No.25, 2011,
- [37] M. Xue, et al., "Absorption and transport enhancement by Ag nanoparticle plasmonics for organic optoelectronics," in *Saudi International Electronics, Communications and Photonics Conference 2011, SIEPCPC 2011*, 2011.
- [38] J. L. Wu, et al., "Upconversion effects on the performance of near-infrared laser-driven polymer photovoltaic devices", *Organic Electronics: physics, materials, applications*, Vol.13, No.10, 2012, pp.2104-2108.
- [39] F. C. Chen, et al., "Plasmonic-enhanced polymer photovoltaic devices incorporating solution-processable metal nanoparticles", *Appl. Phys. Lett.*, Vol.95, No.1, 2009,
- [40] X. Z. Li, et al., "Study of Au/Au<sup>3+</sup>-TiO<sub>2</sub> photocatalysts toward visible photooxidation for water and wastewater treatment", *Environmental Science and Technology*, Vol.35, No.11, 2001, pp.2381-2387.

- [41] Y. Yu, et al., "Single-crystalline TiO<sub>2</sub> nanorods: Highly active and easily recycled photocatalysts", *Applied Catalysis B: Environmental*, Vol.73, No.1-2, 2007, pp.166-171.
- [42] R. Zanella, et al., "Alternative methods for the preparation of gold nanoparticles supported on TiO<sub>2</sub>", *Journal of Physical Chemistry B*, Vol.106, No.31, 2002, pp.7634-7642.
- [43] V. Subramanian, et al., "Catalysis with TiO<sub>2</sub>/Gold Nanocomposites. Effect of Metal Particle Size on the Fermi Level Equilibration", *Journal of the American Chemical Society*, Vol.126, No.15, 2004, pp.4943-4950.
- [44] P. Roy, et al., "TiO<sub>2</sub> nanotubes: Synthesis and applications", *Angewandte Chemie - International Edition*, Vol.50, No.13, 2011, pp.2904-2939.
- [45] N. Talebian, et al., "Comparative study of the structural, optical and photocatalytic properties of semiconductor metal oxides toward degradation of methylene blue", *Thin Solid Films*, Vol.518, No.8, 2010, pp.2210-2215.
- [46] C. H. Wu, et al., "Kinetics of photocatalytic decomposition of methylene blue", *Industrial and Engineering Chemistry Research*, Vol.45, No.19, 2006, pp.6450-6457.
- [47] C. H. Wu, et al., "Decomposition of acid dye by TiO<sub>2</sub> thin films prepared by the sol-gel method", *Industrial and Engineering Chemistry Research*, Vol.45, No.6, 2006, pp.2040-2045.

- [48] A. Pearson, et al., "Gold Nanoparticle-Decorated Keggin Ions/TiO<sub>2</sub> Photocatalyst for Improved Solar Light Photocatalysis", *Langmuir*, Vol.27, No.11, 2011, pp.6661-6667.
- [49] S. D. Sharma, et al., "Photodegradation of dye pollutant under UV light by nano-catalyst doped titania thin films", *Applied Catalysis B: Environmental*, Vol.84, No.1-2, 2008, pp.233-240.
- [50] V. Scuderi, et al., "An enhanced photocatalytic response of nanometric TiO<sub>2</sub>wrapping of Au nanoparticles for eco-friendly water applications", *Nanoscale*, Vol.6, No.19, 2014, pp.11189-11195.
- [51] T. Okuno, et al., "Three modes of high-efficient photocatalysis using composites of TiO<sub>2</sub>-nanocrystallite-containing mesoporous SiO<sub>2</sub> and Au nanoparticles", *J. Sol-Gel Sci. Technol.*, Vol.74, No.3, 2015, pp.748-755.
- [52] A. Ayati, et al., "A review on catalytic applications of Au/TiO<sub>2</sub> nanoparticles in the removal of water pollutant", *Chemosphere*, Vol.107, 2014, pp.163-174.
- [53] W. Zhang, et al., "Photocatalytic activity of Ag nanoparticle-dispersed N-TiO<sub>2</sub> nanofilms prepared by magnetron sputtering", *RSC Advances*, Vol.5, No.70, 2015, pp.57155-57163.

- [54] N. Pugazhenthiran, et al., "Photocatalytic degradation of ceftiofur sodium in the presence of gold nanoparticles loaded TiO<sub>2</sub> under UV-visible light", Chem. Eng. J., Vol.241, 2014, pp.401-409.
- [55] K. Awazu, et al., "A plasmonic photocatalyst consisting of silver nanoparticles embedded in titanium dioxide", J. Am. Chem. Soc., Vol.130, No.5, 2008, pp.1676-1680.
- [56] Y. Tian, et al., "Plasmon-induced photoelectrochemistry at metal nanoparticles supported on nanoporous TiO<sub>2</sub>", Chemical Communications, Vol.10, No.16, 2004, pp.1810-1811.
- [57] S. C. Warren, et al., "Plasmonic solar water splitting", Energy and Environmental Science, Vol.5, No.1, 2012, pp.5133-5146.
- [58] E. Kowalska, et al., "Visible light-induced photocatalytic reaction of gold-modified titanium(IV) oxide particles: Action spectrum analysis", Chemical Communications, No.2, 2009, pp.241-243.
- [59] E. Kowalska, et al., "Visible-light-induced photocatalysis through surface plasmon excitation of gold on titania surfaces", Physical Chemistry Chemical Physics, Vol.12, No.10, 2010, pp.2344-2355.
- [60] E. Fortunato, et al., "Transparent conducting oxides for photovoltaics", MRS Bull., Vol.32, No.3, 2007, pp.242-247.

- [61] A. B. V. Kiran Kumar, et al., "Silver nanowire based flexible electrodes with improved properties: High conductivity, transparency, adhesion and low haze", *Mater. Res. Bull.*, Vol.48, No.8, 2013, pp.2944-2949.
- [62] A. Kumar, et al., "The race to replace tin-doped indium oxide: Which material will win?", *ACS Nano*, Vol.4, No.1, 2010, pp.11-14.
- [63] D. J. Lipomi, et al., "Skin-like pressure and strain sensors based on transparent elastic films of carbon nanotubes", *Nature Nanotechnology*, Vol.6, No.12, 2011, pp.788-792.
- [64] S. Kirchmeyer, et al., "Scientific importance, properties and growing applications of poly(3,4-ethylenedioxythiophene)", *J. Mater. Chem.*, Vol.15, No.21, 2005, pp.2077-2088.
- [65] G. Eda, et al., "Large-area ultrathin films of reduced graphene oxide as a transparent and flexible electronic material", *Nature Nanotechnology*, Vol.3, No.5, 2008, pp.270-274.
- [66] L. Hu, et al., "Percolation in transparent and conducting carbon nanotube networks", *Nano Lett.*, Vol.4, No.12, 2004, pp.2513-2517.
- [67] J. Li, et al., "Organic light-emitting diodes having carbon nanotube anodes", *Nano Lett.*, Vol.6, No.11, 2006, pp.2472-2477.

- [68] K. S. Kim, et al., "Large-scale pattern growth of graphene films for stretchable transparent electrodes", *Nature*, Vol.457, No.7230, 2009, pp.706-710.
- [69] Z. Wu, et al., "Transparent, conductive carbon nanotube films", *Science*, Vol.305, No.5688, 2004, pp.1273-1276.
- [70] M. Zhang, et al., "Materials science: Strong, transparent, multifunctional, carbon nanotube sheets", *Science*, Vol.309, No.5738, 2005, pp.1215-1219.
- [71] S. Bae, et al., "Roll-to-roll production of 30-inch graphene films for transparent electrodes", *Nature Nanotechnology*, Vol.5, No.8, 2010, pp.574-578.
- [72] F. Bonaccorso, et al., "Graphene photonics and optoelectronics", *Nature Photonics*, Vol.4, No.9, 2010, pp.611-622.
- [73] D. S. Hecht, et al., "Emerging transparent electrodes based on thin films of carbon nanotubes, graphene, and metallic nanostructures", *Adv. Mater.*, Vol.23, No.13, 2011, pp.1482-1513.
- [74] C. Niu, "Carbon nanotube transparent conducting films", *MRS Bull.*, Vol.36, No.10, 2011, pp.766-773.
- [75] S. De, et al., "Silver nanowire networks as flexible, transparent, conducting films: Extremely high DC to optical conductivity ratios", *ACS Nano*, Vol.3, No.7, 2009, pp.1767-1774.

- [76] H. Wu, et al., "Electrospun metal nanofiber webs as high-performance transparent electrode", *Nano Lett.*, Vol.10, No.10, 2010, pp.4242-4248.
- [77] J. Van De Groep, et al., "Transparent conducting silver nanowire networks", *Nano Lett.*, Vol.12, No.6, 2012, pp.3138-3144.
- [78] V. Scardaci, et al., "Spray deposition of highly transparent, low-resistance networks of silver nanowires over large areas", *Small*, Vol.7, No.18, 2011, pp.2621-2628.
- [79] E. C. Garnett, et al., "Self-limited plasmonic welding of silver nanowire junctions", *Nature Materials*, Vol.11, No.3, 2012, pp.241-249.
- [80] P. E. Lyons, et al., "High-performance transparent conductors from networks of gold nanowires", *Journal of Physical Chemistry Letters*, Vol.2, No.24, 2011, pp.3058-3062.
- [81] D. S. Leem, et al., "Efficient organic solar cells with solution-processed silver nanowire electrodes", *Adv. Mater.*, Vol.23, No.38, 2011, pp.4371-4375.
- [82] L. Hu, et al., "Metal nanogrids, nanowires, and nanofibers for transparent electrodes", *MRS Bull.*, Vol.36, No.10, 2011, pp.760-765.
- [83] M. G. Kang, et al., "Organic solar cells using nanoimprinted transparent metal electrodes", *Adv. Mater.*, Vol.20, No.23, 2008, pp.4308-4313.

- [84] J. Israelachvili, "Intermolecular and surface forces" (Academic, N. Y), 1992.
- [85] S. Dietrich, "Phase Transition and critical phenomena" (Academic, London), 1988.
- [86] K. Jacobs and S. Herminghaus, "Thin liquid polymer films rupture via defects", *Langmuir*, Vol.14, No.4, pp.965-969, 1988
- [87] W. W. Mullins, "Flattening of a Nearly Planar Solid Surface Due to Capillarity:" *J. Appl. Phys.* 30, 77 1959.
- [88] D. J. Srolovitz, et al., "Capillary instabilities in thin films. II. Kinetics", *J. Appl. Phys.*, Vol.60, No.1, 1986, pp.255-260.
- [89] D. T. Danielson, et al., "Surface-energy-driven dewetting theory of silicon-on-insulator agglomeration", *J. Appl. Phys.*, Vol.100, No.8, 2006,
- [90] A. Schaub, et al., "Gold nanolayer and nanocluster coatings induced by heat treatment and evaporation technique", *Nanoscale Research Letters*, Vol.8, No.1, 2013, pp.1-8.
- [91] F. Niekiel, et al., "The process of solid-state dewetting of Au thin films studied by in situ scanning transmission electron microscopy", *Acta Mater.*, Vol.90, 2015, pp.118-132.
- [92] D. Wang, et al., "Formation of precise 2D Au particle arrays via thermally induced dewetting on pre-patterned substrates", *Beilstein Journal of Nanotechnology*, Vol.2, No.1, 2011, pp.318-326.

- [93] J. W. Leem, et al., "Antireflective characteristics of disordered GaAs subwavelength structures by thermally dewetted Au nanoparticles", *Sol. Energy Mater. Sol. Cells*, Vol.95, No.2, 2011, pp.669-676.
- [94] J. Mizsei, et al., "In situ AFM, XRD and resistivity studies of the agglomeration of sputtered silver nanolayers", *J. Nanopart. Res.*, Vol.3, No.4, 2001, pp.271-278.
- [95] C. M. Müller, et al., "Microstructure evolution during dewetting in thin Au films", *Acta Mater.*, Vol.58, No.18, 2010, pp.6035-6045.
- [96] A. D. Rakić, et al., "Optical properties of metallic films for vertical-cavity optoelectronic devices", *Appl. Opt.*, Vol.37, No.22, 1998, pp.5271-5283.
- [97] S. H. Kwon, et al., "Mechanism of solid-state plasma-induced dewetting for formation of copper and gold nanoparticles", *Journal of Nanoscience and Nanotechnology*, Vol.13, No.9, 2013, pp.6109-6114.
- [98] N. Sardana, et al., "Surface plasmons on ordered and bi-continuous spongy nanoporous gold", *New Journal of Physics*, Vol.16, 2014,
- [99] C. An, et al., "Plasmonic enhancement of photocatalysis over Ag incorporated AgI hollow nanostructures", *RSC Advances*, Vol.4, No.5, 2014, pp.2409-2413.
- [100] J. Li, et al., "A study of photodegradation of sulforhodamine B on

Au-TiO<sub>2</sub>/bentonite under UV and visible light irradiation", Solid State Sciences, Vol.11, No.12, 2009, pp.2037-2043.

## VI. 국문 초록

고상 디웨팅은 물질의 녹는점 이하에서 외부에서 가해지는 에너지에 의해 박막이 파티클로 이루어진 어레이가 되는 물리적 현상을 뜻한다. 그 중에서도 플라즈마를 이용한 디웨팅 방법은 잘 알려진 열처리 디웨팅이나 펄스 레이저를 이용한 디웨팅에 비해 다양한 장점을 가진다. 저온 공정, 빠른 공정 속도 및 대면적 공정이 가능하며, 균일한 크기 및 분포를 가진 파티클 어레이를 제조 할 수 있다. 플라즈마를 이용한 디웨팅의 경우, 박막에 입사되는 이온의 충돌 효과 및 박막 표면에 직접적인 에너지 전달 방식 덕분에 홀 뉴클리에이션이 활발히 일어난다. 따라서 균일한 파티클 크기를 가진 어레이를 만들 수 있으며 공정 속도 또한 빠르게 진행된다.

본 연구에서는 금, 은, 구리 같은 플라즈몬 특성을 나타낼 수 있는 금속들을 선택하여 플라즈마 처리를 이용해 성공적으로 박막을 금속 나노 파티클 어레이로 성공적으로 제조하였고 플라즈마 처리 시간에 따른 디웨팅 변화 과정의 메커니즘을 분석하였다. FESEM 사진 분석을 통해 디웨팅 과정을 나타낼 수 있는 기판이 드러나는 면적을 수치화하여 계산하고 스침각 입사 소각 엑스선 산란을 이용하여 결정학적 변화 과정을 분석하였다.

다양한 나노 파티클 어레이 분포를 만들기 위하여 박막 두께, 플라즈마 처리 시간, 박막 밀도, 박막과 기판 사이 계면 에너지 등의

다양한 변수가 고려되었다. 이러한 변수들에 의해 나노 파티클의 사이즈, 파티클 간의 간격, 단위 면적 당 파티클의 개수, 디웨팅 완료까지 걸리는 시간 등을 조절할 수 있었으며 특히, 디웨팅 공정의 반복을 이용하여 나노 파티클 어레이의 분포에 상당한 변화를 줄 수 있는 방법을 소개하였다. 이러한 플라즈마 디웨팅을 이용하여 만들어진 나노 구조를 유기 태양전지, 이산화티타늄의 광촉매 활성 효과 및 금속 투명 전도막 분야에 적용하였다.

플라즈몬 증강 흡수 효과에 의해 유기태양전지의 효율을 높이기 위해 산화인듐주석에 금 나노 파티클 어레이를 제조하였다. 금의 플라즈몬 공명 주파수와 유기 태양전지의 흡수띠 영역을 맞추기 위해 다양한 분포를 가진 어레이를 적용 시키고 이를 통해 에너지 변환 효율을 극대화 시키는 최적의 조건을 제시하였다. 뿐만 아니라 금 나노 파티클 어레이를 이산화티타늄 표면에 제조하여 메틸렌블루의 광분해 효과를 자외선 영역과 가시광선 영역에서 각각 평가하였다. 특히, 반복적인 디웨팅을 이용하여 제조한 나노 파티클의 개수 밀도가 높은 시편에서 성공적인 결과를 얻었다. 마지막으로 바이컨티뉴어스 구조를 금속 투명 전도막에 적용하였다. 금속 투명 전도막의 주요 인자인 시트 저항과 광투과율을 금 박막의 두께 및 플라즈마 처리시간을 조절하여 평가하였다. 플라즈마를 이용한 디웨팅은 간단하고 빠르고 효율적인 공정으로 금속 투명 전도막으로써 적용가능성을 확인할 수 있었다.